

The Influence of Geomagnetic Storms on Calculating Magnetotelluric Impedance

Hao Chen (✉ chenhaomagnetic@gmail.com)

Kyushu university <https://orcid.org/0000-0002-1944-2605>

Hideki Mizunaga

Kyushu University - Ito Campus: Kyushu Daigaku

Toshiaki Tanaka

Kyushu University - Ito Campus: Kyushu Daigaku

Research Article

Keywords: geomagnetic storm, impedance tensor, magnetotelluric method

Posted Date: May 26th, 2021

DOI: <https://doi.org/10.21203/rs.3.rs-542900/v1>

License: © ⓘ This work is licensed under a Creative Commons Attribution 4.0 International License.

[Read Full License](#)

26 noise ratio (SNR) is low. Geomagnetic storms represent temporary disturbances of the Earth's
27 magnetosphere caused by solar wind-shock wave interacts with Earth's magnetic field. The
28 variation of the electromagnetic signal increases dramatically in the presence of a strong
29 geomagnetic storm. Using the data observed during a strong geomagnetic storm may overcome
30 the locale noise and bring a reliable MT impedance at contaminated sites. Three case studies are
31 presented to show the positive effect of geomagnetic storms on MT field data. A more reliable
32 and interpretable impedance calculated from a survey line contaminated by strong noise is
33 obtained using the data observed during a strong geomagnetic storm.

34

35 Keywords: geomagnetic storm, impedance tensor, magnetotelluric method

36

37 **1 INTRODUCTION**

38 The magnetotelluric method is a passive electromagnetic (EM) method used to infer the
39 subsurface electrical conductivity from the natural geomagnetic and geoelectric fields observed
40 at Earth's surface. It was first proposed by Rikitake (1948), Cagniard (1953) and Tikhonov
41 (1950). The natural MT sources from the Earth's magnetosphere and ionosphere or global
42 lighting are far enough from the observation site. Therefore, we can treat the EM signals as
43 plane waves. Many works have focused on the Earth's EM environment (Constable, 2016;
44 Constable and Constable, 2004; McPherron, 2005). Generally, the low-frequency signals (< 1
45 Hz) originate from the interaction between solar winds and the Earth's magnetosphere and
46 ionosphere. In comparison, high-frequency signals (> 1 Hz) originate from worldwide
47 thunderstorm activity. Constable (2016) reviewed EM sources in high frequencies band (> 1 Hz).
48 McPherron (2005) reviewed the ultralow frequency (ULF) band EM source. Garcia (2002) used
49 MT data to research the characteristics of EM signals in the high-frequency band. The MT field
50 data include natural EM signals and noise. Szarka (1988) and Junge (1996) summarized the
51 active and passive noise sources observed in MT measurements. Not all MT time series include

52 usable information about the electrical conductivity distribution at depth, particularly when the
53 signal-to-noise ratio is low. It can occur when the natural signal level is comparable to or below
54 the instrument noise level or in the presence of some types of cultural noise (Chave and Jones,
55 2012). The first step in MT data processing is to estimate the frequency-domain impedance
56 tensor from the measured time-series data. All MT data interpretations are based on the MT
57 impedance. Therefore, it is very important to obtain a reliable impedance. The low signal-to-
58 noise ratio data can be regarded as noisy data. Robust procedures can only obtain reliable
59 impedance from a reasonable proportion of noisy data, i.e., typically no more than 40-50%
60 (Smirnov, 2003).

61 The effect of lightning and geomagnetic storms on MT data is well understood. From the
62 perspective of the signal-to-noise ratio (SNR), Hennessy and Macnae (2018) reduced the
63 impedance bias by stitching the highest amplitude audio-frequency MT (AMT) time-series data,
64 which corresponds to lightnings. During a strong geomagnetic storm, the variation in the natural
65 EM signal increases substantially. Sometimes, the amplitude of EM signals during the strong
66 storm can be 100 times greater than during the non-storm period. Noise can be neglected under
67 this condition. The noisy data segment is converted to high signal-to-noise ratio data, depending
68 on the strength of the geomagnetic storm and the noise. However, the plane-wave assumption of
69 the MT is violated at high magnetic latitudes because the source field is nonuniform during
70 geomagnetic storms (Mareschal, 1981; Viljanen et al., 1993; Garcia et al., 1997; Lezaeta et al.,
71 2007). Possible biases in the MT transfer function due to the source effect are considered only at
72 long periods (> 1000 s) and near the auroral or equatorial electrojets (Murphy and Egbert, 2018).
73 The plane wave assumption is generally acceptable at midlatitudes (Lezaeta et al., 2007;
74 Viljanen et al., 1993). This paper used three field datasets at mid-latitudes to research the
75 influence of geomagnetic storms on MT data.

76 In this paper, a statistical analysis of geomagnetic storm was performed first in section 2.
77 Section 3 introduces the parameters and the impedance estimator used in the research. Section 4

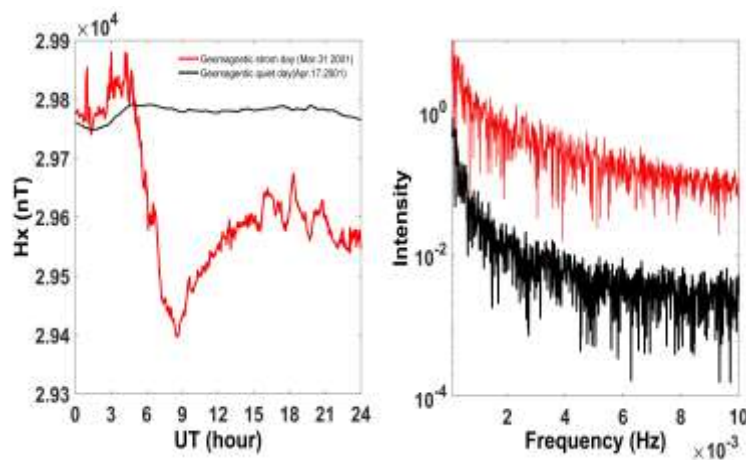
78 shows three case studies influenced by geomagnetic storms.

79 In the practical MT surveys, we may meet the noisy sites occasionally that can't obtain a
80 reliable impedance by the current method. When we redo the MT surveys at noisy sites, we may
81 acquire MT data during strong geomagnetic storms. Although strong geomagnetic storms do not
82 occur frequently, we could predict strong geomagnetic storms using space weather forecasts and
83 acquire MT data during intense geomagnetic storms. Using the data observed during the intense
84 storm period may bring a reliable result from the site contaminated with continuous noise.

85

86 2 GEOMAGNETIC STORM

87



88

89 Fig. 1 The geomagnetic intensities along the N-S direction during a storm day and a non-storm
90 day. The black lines denote the non-storm day's data, and the red lines denote the storm day's data.
91 The left is a profile in the time domain, and the right is a profile in the frequency domain.

92

93 The geomagnetic storm is a temporary disturbance of the Earth's magnetosphere caused by a solar
94 wind shock wave interacts with the Earth's magnetic field. Geomagnetic storms start when the
95 enhanced energy of the solar wind transfer into the magnetosphere. A magnetic storm is seen as a
96 rapid drop in the magnetic field strength at the Earth's surface. Fig.1 shows the X (N-S)

97 component of the geomagnetic field during a storm day and a non-storm day at the Kakioka
98 (KAK) station in Japan. In 1973, the KAK Magnetic Observatory was designated as one of four
99 facilities to calculate the disturbance storm time (Dst) index, representing the strength of the
100 equatorial ring current encircling the Earth. The intensity of the magnetic field observed during
101 the storm day can be almost two orders stronger than during the non-storm day.

102 The disturbance storm time (Dst) index is a negative index of geomagnetic activity used to
103 estimates the averaged change of the horizontal component of the Earth's magnetic field based on
104 measurements from a few magnetometer stations. It is derived from hourly scalings of low-
105 latitude horizontal magnetic variation and expressed in nanoteslas. When the Dst index is less
106 than -50 nT, it is categorized as a geomagnetic storm. When the Dst index is less than -100 nT, it
107 is categorized as a strong geomagnetic storm. In this section, we analyzed the geomagnetic storm
108 event statistically by the Dst index.

109 Fig. 2 shows the distribution of the Dst index from 1957 to 2020; the orange line denotes the
110 boundary of the geomagnetic storm ($Dst \leq -50$ nT), and the light blue line denotes the boundary
111 of the strong geomagnetic storm ($Dst \leq -100$ nT). It shows that geomagnetic storms did not
112 appear frequently. The probability of a strong storm is less than 1% per day.

113 Fig. 3 shows the statistical analysis of each strong geomagnetic storm event by the hour. The
114 upper figure shows the number of strong geomagnetic storm events versus the strong storm
115 event's length by the hour. The horizontal axis denotes the length of the strong storm event, and
116 the y-axis denotes the number. The lower figure shows the cumulative distribution of the upper
117 figure. It shows that about 46% of strong geomagnetic events lasted more than 4 hours, and 8% of
118 the strong geomagnetic event lasted more than one day. The longest strong geomagnetic event
119 lasted 55 hours. There are 688 strong geomagnetic storms from 1957 to 2020; one year had about
120 ten strong geomagnetic events, and about five events lasted more than 4 hours on average.

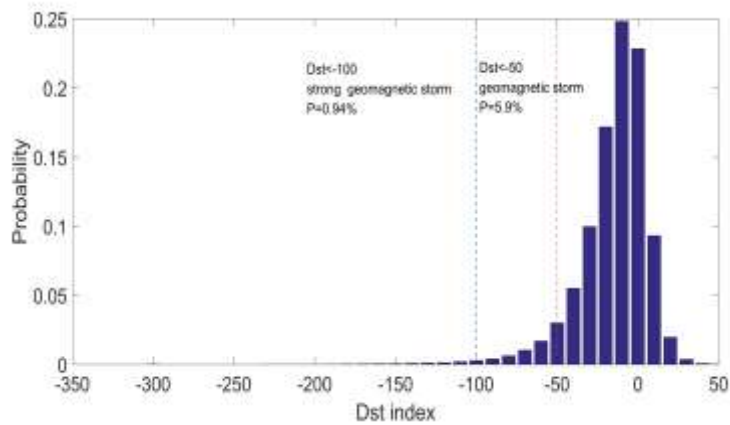
121 Fig. 4 shows the monthly count of strong geomagnetic storms. One hour was recorded as one
122 count in this figure. For example, a 3-hour storm is counted as three storms. The high probability

123 of a strong geomagnetic storm occurred around April and October.

124 Fig. 5 shows the yearly count of geomagnetic storms that occurred in each year. Fig.6 shows
125 the FFT result of the yearly count of storms from 1957 to 2020. There is a 10.7-year peak, which
126 corresponds to the 11-year solar cycle.

127 This section concludes that the geomagnetic storm has a seasonal and 11-year solar cycle. The
128 strong geomagnetic storm doesn't happen frequently and causes significant EM field variations
129 observed on the Earth's surface.

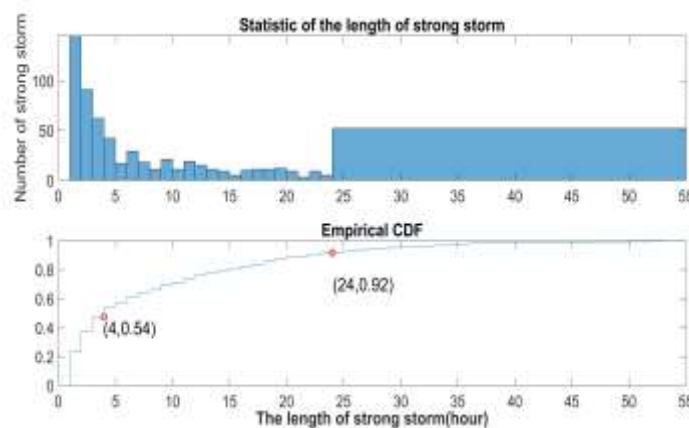
130



131

132 Fig. 2 The distribution of strong storms based on the Dst index between 1957 - 2020, the orange
133 line denotes Dst (≤ -50 nT), and the light blue line denotes Dst (≤ -100 nT).

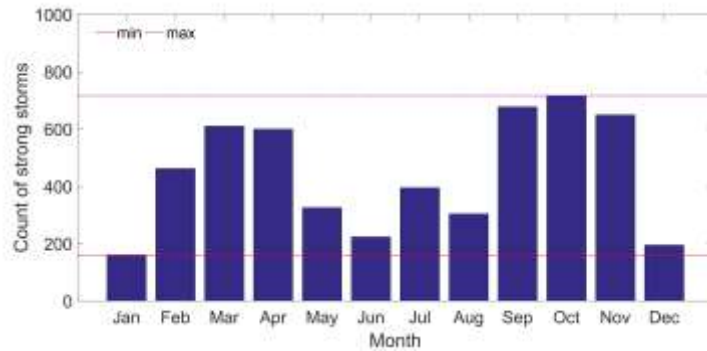
134



135

136 Fig. 3 The statistical analysis of each strong geomagnetic storm event. The upper figure shows the

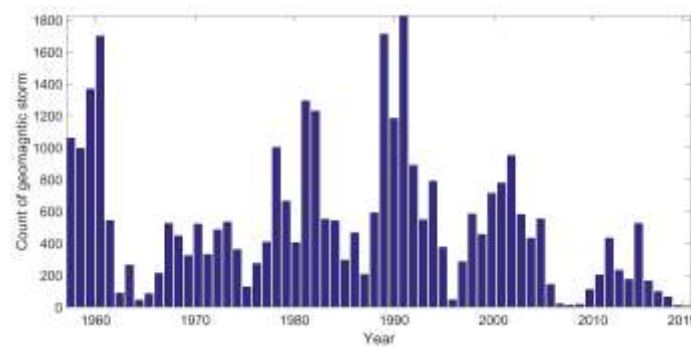
137 number of each strong geomagnetic storm event in a different storm event length. The lower
138 figure shows the cumulative distribution of the upper figure.



139

140 Fig. 4 The monthly count of strong geomagnetic storms based on the Dst index.

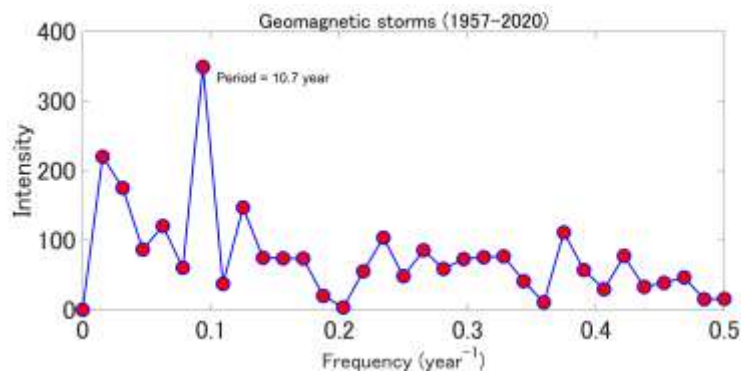
141



142

143 Fig. 5 The yearly count of geomagnetic storms based on the Dst index from 1957 to 2020.

144



145

146 Fig. 6 The calculated periods by Fourier analysis using the yearly count of geomagnetic storms

147 from 1957 to 2020.

148 3 METHOD

149 We introduce the method to estimate the influence of geomagnetic storms on the MT data in this
150 section. At first, we introduce two MT impedance estimators. And then, introduce the linear
151 coherency (RLcoh) and amplitude ratio (R_AR) between the local and remote magnetic field and
152 polarization direction to discuss the data quality at the noisy site KAP03 133. Finally, We also
153 investigate the influence of geomagnetic storms based on cross-power spectra and coherency
154 distribution.

155

156 3.1 Impedance Tensor Estimator

157 In the MT method, the magnetic field (\mathbf{H}) and the electric field (\mathbf{E}) have a linear relationship
158 in the frequency domain. The impedance tensor at a specific frequency can be calculated in the
159 frequency domain as follows:

$$160 \begin{pmatrix} E_x(\omega) \\ E_y(\omega) \end{pmatrix} = \begin{pmatrix} Z_{xx}(\omega) & Z_{xy}(\omega) \\ Z_{yx}(\omega) & Z_{yy}(\omega) \end{pmatrix} \begin{pmatrix} H_x(\omega) \\ H_y(\omega) \end{pmatrix}, \quad (1)$$

161 where E and H are the horizontal electric and magnetic field at a specific frequency, respectively,
162 ω denotes the angular frequency, and Z means the MT impedance. The suffix x denotes the north-
163 south direction, and y denotes the east-west direction.

164 Bounded Influence Remote Reference Processing (BIRRP; Chave and Thomson, 2004) is a
165 typical conventional robust estimator to calculate the impedance tensor based on windowed FFT.
166 In this paper, we mainly show the impedance calculated by BIRRP.

167 There is an issue that the natural EM signal may be nonstationary during the geomagnetic
168 storm. It is not suitable for the basic requirements of conventional methods based on the Fourier
169 transform and leads the impedance biased. In this research, we also used a nonstationary
170 processing routine named EMT (Neukirch et al., 2014) to calculate the impedance at the quiet site
171 Kap03-163. The biggest difference between EMT and BIRRP is that EMT transforms the time
172 series into the frequency domain by the time-frequency transform technique Hilbert-Huang

173 Transform (HHT) and can estimate MT response functions even in the presence of nonstationary
174 (NS) signal.

175

176 **3.2 The Linear Coherency and Amplitude Ratio between the Local and Remote Magnetic** 177 **field**

178 More than four channels are observed simultaneously in MT fieldwork; the time series of each
179 channel is divided into N segments, and N spectra can be obtained from these N segments by
180 applying the Fourier transform to each channel.

181 In polar coordinates, the cross-power spectra are expressed as follows:

$$182 \quad A_i \bar{B}_i = |A_i| \cdot |B_i| e^{j(\varphi_{A_i} - \varphi_{B_i})}, \quad (2)$$

183 where j denotes the imaginary number unit, $i=1,2,\dots, N$; A_i and B_i are the spectra calculated from
184 the i^{th} segment from the different channel; and φ_{A_i} and φ_{B_i} denote the phases of A_i and B_i ,
185 respectively. The overline denotes the complex conjugate.

186 The amplitude of the cross-power spectra equal the product of $|A_i|$ and $|B_i|$, and the phase equals
187 the phase difference (PD) between A_i and B_i .

188 The auto-power spectra are calculated as follows:

$$189 \quad A_i \bar{A}_i = |A_i|^2, \quad B_i \bar{B}_i = |B_i|^2. \quad (3)$$

190 The PD is calculated as follows:

$$191 \quad \theta_i = \varphi_{A_i} - \varphi_{B_i} = \arg(e^{j(\varphi_{A_i} - \varphi_{B_i})}) = \arg\left(\frac{A_i \bar{B}_i}{\sqrt{(A_i \bar{A}_i)(B_i \bar{B}_i)}}\right), \quad (4)$$

192 where θ_i denotes the angle of the PD between the two spectra at a specific frequency.

193 The linear coherency is proposed as the cosine of the PD as follows:

$$194 \quad Lcoh = \cos(\theta_i) = \text{Re}(e^{j(\varphi_{A_i} - \varphi_{B_i})}) = \text{Re}\left(\frac{A_i \bar{B}_i}{\sqrt{(A_i \bar{A}_i)(B_i \bar{B}_i)}}\right), \quad (5)$$

195 where Lcoh denotes the linear coherency and Re denotes the real part of the complex number.

196 The value of Lcoh lies in the range of (-1,1). When the PD is close to 0° , the Lcoh value is high

197 and close to 1. According to Euler's formula, Lcoh is also equal to the real part of $e^{j(\varphi_{A_i} - \varphi_{B_i})}$.

198 If there is a remote site available, for the north-south direction, the linear coherency between
 199 the remote and local magnetic fields (RLcoh) is defined as follows:

$$200 \quad \text{RLcoh} = \text{Re} \left(\frac{H_{x_i} \bar{H}_{xr_i}}{\sqrt{(H_{x_i} \bar{H}_{x_i})(H_{xr_i} \bar{H}_{xr_i})}} \right), \quad (6)$$

201 where H_{x_i} and H_{xr_i} are the local and remote magnetic field spectra at a specific frequency
 202 calculated from the i^{th} segment.

203 The field MT data include natural EM signals and noise coming from the local environment.

204 We can rewrite the magnetic field H as follows:

$$205 \quad H = H^{\text{MT}} + H^{\text{N}},$$

$$206 \quad H_r = H_r^{\text{MT}} + H_r^{\text{N}}, \quad (7)$$

207 where N denotes the noise and MT denotes the natural EM signals coming from the
 208 magnetosphere and ionosphere.

209 The portion of the natural magnetic signals in the local (H^{MT}) and remote sites (H_r^{MT}) comes
 210 from the same source. The H^{MT} and H_r^{MT} values should be similar to each other, indicating that
 211 the amplitudes and phases of the spectra should be comparable.

212 When the signal-to-noise ratio (SNR) is high at both local and remote sites, the PD between
 213 the local and remote magnetic fields should be close to 0° , and the RLcoh value should be close
 214 to one. The amplitude ratio (AR) between the local and remote magnetic fields (R_AR) is
 215 calculated as follows:

$$216 \quad R_{\text{AR}} = \frac{|H^{\text{MT}}|}{|H_r^{\text{MT}}|}, \quad (8)$$

217 the R_AR value should be low and close to one.

218 In contrast, in the presence of strong noise, the PD between the local and remote magnetic
 219 fields will be scattered; therefore, the RLcoh will be unstable; and the R_AR value will deviate
 220 from one.

221 RLcoh and R_AR are parameters to measure the similarity between the remote and local

222 magnetic fields. If there is a quiet remote reference site, we could use RLcoh and R_AR to
 223 evaluate the variation of SNR change with time at the local site.

224

225 3.3 Polarization Directions

226 Weckmann et al. (2005) showed the effectiveness of using the polarization directions to
 227 estimate the background noise. The polarization directions for the electric field (α_E) and magnetic
 228 field (α_H) (Fowler et al., 1967) at a specific frequency are defined as:

$$229 \quad \alpha_{E,i} = \tan^{-1} \frac{2\text{Re}[E_{x,i}\bar{E}_{y,i}]}{[E_{x,i}\bar{E}_{x,i}] - [E_{y,i}\bar{E}_{y,i}]}, \quad (9)$$

$$230 \quad \alpha_{H,i} = \tan^{-1} \frac{2\text{Re}[H_{x,i}\bar{H}_{y,i}]}{[H_{x,i}\bar{H}_{x,i}] - [H_{y,i}\bar{H}_{y,i}]}. \quad (10)$$

231 We can rewrite the polarization directions as follows:

$$232 \quad \tan^{-1} \frac{2\text{Re}[A_i\bar{B}_i]}{[A_i\bar{A}_i] - [B_i\bar{B}_i]} = \tan^{-1} \frac{2\frac{|B_i|}{|A_i|}\cos(\theta_i)}{1 - \left(\frac{|B_i|}{|A_i|}\right)^2}, \quad (11)$$

233 where A_i and B_i are $H_{x,i}$ and $H_{y,i}$ or $E_{x,i}$ and $E_{y,i}$, respectively. The polarization direction is
 234 related to the PD and amplitude ratio (AR) between the two orthogonal fields. A variety of
 235 sources generate natural magnetic signals. These sources generate magnetic fields that vary in
 236 their incident directions. The PD and amplitude ratio between the two orthogonal magnetic fields
 237 vary with time; thus, there is no preferred polarization direction for the magnetic field. However,
 238 according to a given conductivity distribution in the subsurface, a preferred polarization direction
 239 may exist for the induced electric field (Weckmann et al., 2005).

240

241 3.4 Ordinary Coherency

242 The coherency is a quantitative measure of the phase difference (PD) consistency between the
 243 two channels. If two channels are coherent, their phases must be either the same or have a
 244 constant difference (Marple and Marino, 2004). Coherency is defined as the ratio between cross-
 245 power spectra density and the root of auto powers spectra density. For A and B spectrum at a

246 specific frequency, it is defined as:

$$247 \quad \text{Coh}(A, B) = \frac{|\langle A\bar{B} \rangle|}{\sqrt{\langle A\bar{A} \rangle \langle B\bar{B} \rangle}}, \quad (12)$$

248 where the brackets represent the averages of N individual auto power spectra and cross-power
249 spectra. For instance,

$$250 \quad \langle A\bar{B} \rangle = \frac{1}{N} \sum_{i=1}^N A_i \bar{B}_i. \quad (13)$$

251

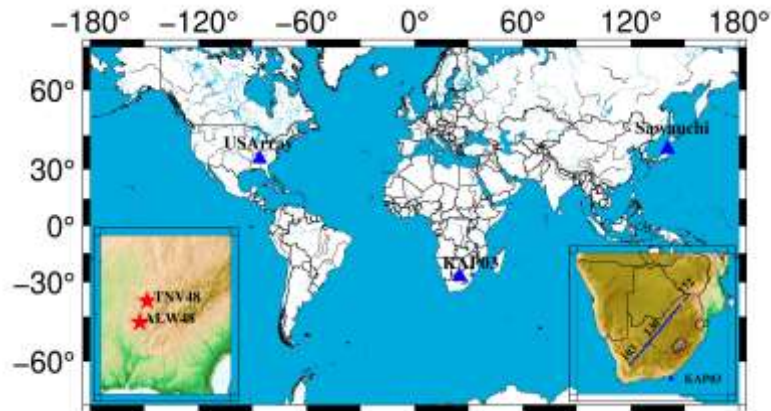
252 **4 CASE STUDIES**

253 Three case studies are shown to evaluate the influence of geomagnetic storms on the MT data.
254 Fig. 7 shows the map of site locations in the three case studies (Sawauchi, USArray, KAP03). The
255 left map shows a detailed map of the site location used in USArray, and the right map shows the
256 detailed survey line of KAP03. All of the case studies include geomagnetic storm data.

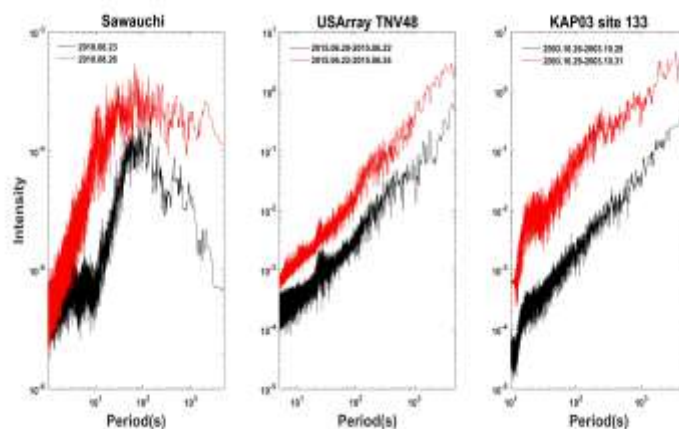
257 Fig. 8 shows the spectrum calculated by the Hx component observed during storm and non-
258 storm days in the three case studies. We used the moving median filter to smooth the spectra. The
259 magnetic coils are used to observe the magnetic field at Sawauchi station, and we need to
260 calibrate to the spectrum. The fluxgate magnetometer is used in the USArray and KAP03 project,
261 and the calibration factor is 1. Because we have not calibrated the spectrum observed at the
262 Sawauchi station, its intensity is smaller than that observed in the USArray and KAP03 projects.
263 During the storm day, the intensity is approximately five times stronger than that measured during
264 the non-storm days between 10 and 1000 seconds at Sawauchi and USArray project. Moreover,
265 the intensity is approximately 50 times stronger than that during non-storm days between 10 and
266 1000 seconds in KAP03.

267 Table 1 shows the name of each result and the corresponding data used to calculate the
268 impedance in studies 2 and 3. The Quiet parameter was calculated using the data observed during
269 the non-storm period, and QuietRR was calculated using the data observed during the non-storm
270 period and using the remote reference technique. The Storm parameter was calculated using the

271 data observed during the storm. StormRR was calculated using the data observed during the
 272 storm period and using the remote reference technique. The period shows the month and day of
 273 the data. For example, 06.20-06.22 means the time from June 20 00:00:00 to June 22 00:00:00.
 274 The geomagnetic storm of USArray occurred in 2015. The geomagnetic storm of KAP occurred
 275 in 2003.



276
 277 Fig. 7 The location map in the three case studies (KAP03, USArray, Sawauchi). The left map
 278 shows the detailed site location used in USArray, and the right map shows the survey line of
 279 KAP03.
 280



281
 282 Fig. 8 Comparison of the spectrum calculated by the Hx component observed during the storm
 283 and non-storm days. The black lines denote the non-storm day's data, and the red lines denote the
 284 storm day's data. The horizontal axis denotes the period. The vertical axis denotes the intensity.

285

286 Table 1 The classification of results and the corresponding data used to calculate MT impedances.

Local Site	Quiet	QuietRR		Storm	StormRR	
	Period	Remote Site	Period	Period	Remote Site	Period
TNV48	06.20-06.22	ALW48	06.20-06.22	06.22-06.24	ALW48	06.22-06.24
KAP 130	11.06-11.10	KAP 163	11.06-11.10	10.29-10.31		
KAP 133	10.26-10.28	KAP 103	11.11-11.18	10.29-10.31		
KAP 136	11.06-11.10	KAP 163	11.06-11.10	10.29-10.31		
KAP 139	11.06-11.10	KAP 163	11.06-11.10	10.29-10.31		
KAP 142	10.25-10.27	KAP 160	11.14-11.20	10.29-10.31		
KAP 145	11.06-11.10	KAP 163	11.06-11.10	10.29-10.31		
KAP 163	11.01-11.04			10.29-10.31		

287

288 **4.1 Case Study 1: Sawauchi, Japan**

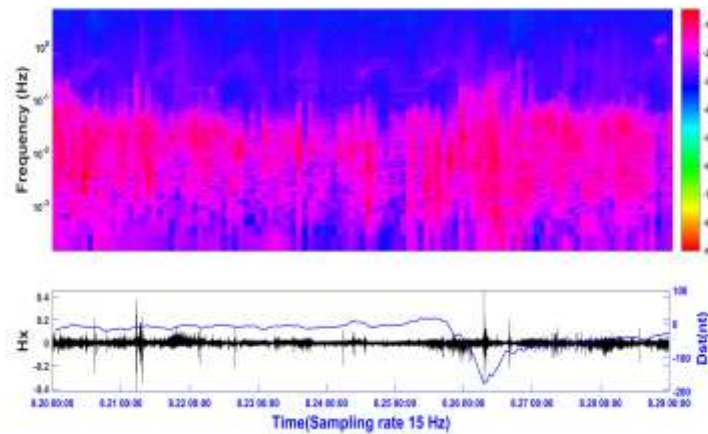
289 The Phoenix geophysics system's broadband frequency 5-component MT time-series data were
290 used in the first case study. The data were observed from August 20 to August 28, 2018, at
291 Sawauchi station, Japan. The geomagnetic storm occurred on August 26. The MT time-series data
292 were stored in three files. Two files sampled the high- and middle-frequency bands (2,400 and
293 150 Hz) intermittently; the other files continuously sampled the low-frequency data (15 Hz). The
294 high-frequency band (2,400 Hz) was sampled for 1 second at intervals of 4 minutes from the
295 beginning of the minute, and the middle-frequency band (150 Hz) was sampled for 16 seconds at
296 intervals of 4 minutes from the beginning of the minute.

297 First, we analyzed the spectrum variation along with the Dst index. To obtain precise spectral
298 information from these datasets, we first applied a set of Slepian tapers and then used the fast
299 Fourier transform to the time series (Garcia and Jones, 2002). Fig. 9 shows the time-frequency
300 distribution against the Dst index and the Hx component time-series data. The sampling rate is 15
301 Hz, and the upper figure shows the spectrum variation from August 20 to August 28. The color
302 denotes the value of $10 \cdot \log_{10}(\text{amp.})$, and "amp" denotes the spectrum amplitude. The lower
303 figure shows the Hx component time series along with the Dst index. This figure shows that the
304 amplitude between approximately 1 second and 1,000 seconds increases dramatically and is

305 correlated with the geomagnetic storm around August 26. The high-frequency (< 1 Hz) amplitude
306 does not change correlated with the geomagnetic storm.

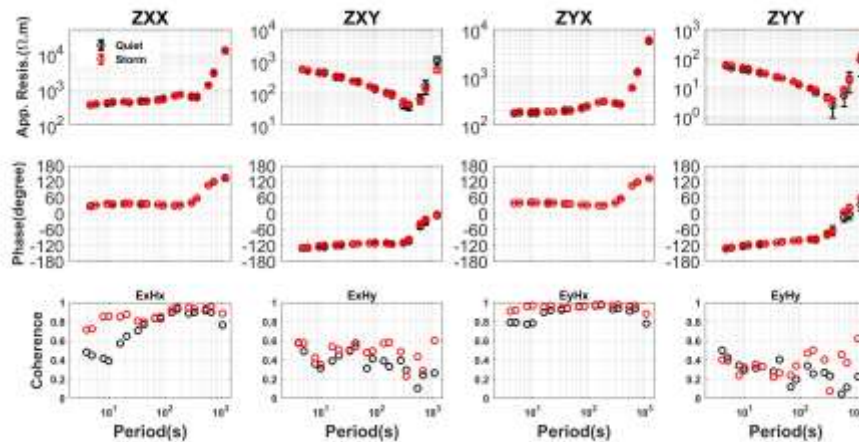
307 We calculated the impedance using each day's data. Fig. 10 shows typical MT sounding curves
308 and the coherency distribution using the data observed during the storm day (August 26) and non-
309 storm day (August 23). The sounding curves calculated using the storm data was more stable than
310 the result using the non-storm data between 300 and 1,000 seconds in the Z_{xy} and Z_{yy}
311 components. The sounding curves of Z_{xx} and Z_{yx} are almost the same. In this result, the phases of
312 the XY component are out of the quadrant. The phenomenon that the phases of off-diagonal
313 impedance tensors exceed the normal quadrants is referred to as phase rolling out of quadrant
314 (PROQ). PROQ can appear in specific geologic environments (Chouteau and Tournerie, 2000;
315 Weckmann et al., 2003; Yu et al., 2018.). The current channeling caused by complex three-
316 dimensional (3-D) isotropic media is one explanation for the PROQ phenomenon. The
317 characteristic of PROQ is that the ordinary coherency between the parallel electric and magnetic
318 field is high, while the coherency between the orthogonal component is low. In Fig. 10, the
319 $\text{Coh}(E_x, H_x)$ value is much higher than the $\text{Coh}(E_x, H_y)$ value. Moreover, the value of $\text{Coh}(E_x, H_x)$
320 increased during the storm period between 4 and 30 seconds. That may have been caused by the
321 increasing intensity of the natural MT signal.

322



323

324 Fig. 9 The time-frequency distribution against the Dst index variation and the sampling rate is 15
 325 Hz. The upper figure shows the time-frequency distribution from August 20 to 29. The color
 326 denotes the value of $10 \cdot \log_{10}$ (amp.). The lower figure shows the time variations of the Hx
 327 component along with the Dst index. The unit of Hx is nT. The horizontal axis denotes the date.
 328
 329



330
 331 Fig. 10 MT sounding curves and coherency distribution during storm days (August 26) and non-
 332 storm days (August 23). The black color indicates the results on the non-storm days; the red color
 333 indicates the storm day results. The upper figures show the apparent resistivity. The four figures
 334 at the middle layer show the impedance phase. The lower figures show the distribution of
 335 coherency. The horizontal axis denotes the period in seconds.
 336

337 Fig. 11 shows the amplitude variation at 16, 8, 4 and 1 second periods along with the Dst index.
 338 The upper figure shows the amplitude variation from August 20 to August 28. The lower figure
 339 shows the time variation of the Hx component along with the Dst index. The amplitude increased
 340 at the 16, 8, and 4 seconds correlated with the geomagnetic storm. In the variation of 1 second,
 341 there was no increase correlated with the storm. This result agrees that the interaction between the
 342 solar wind and the magnetosphere does not contribute to the MT high-frequency signal. The

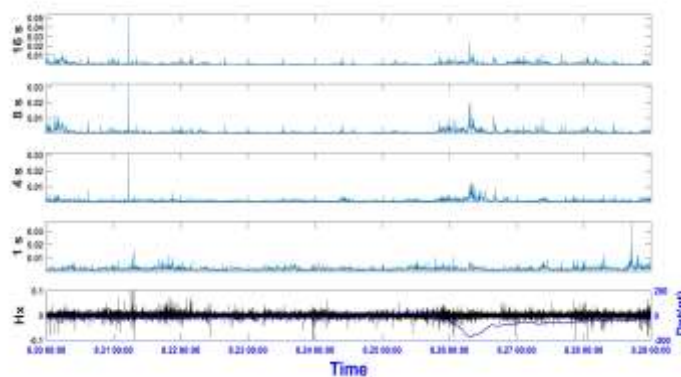
343 signal strength at periods larger than 4 seconds increased dramatically along with the
344 geomagnetic storm. Because the natural EM signal strength between the dead band (0.1-10
345 seconds) is low, and local noise can easily influence it. The enhancement of the natural EM signal
346 may produce a more reliable impedance result. Next, we will investigate the change in impedance
347 value during storm and non-storm days at 10 seconds.

348 Fig. 12 shows the XY component of the impedance value calculated by each day's data at a
349 period of 10 seconds. Usually, the impedance corresponds to the underground resistivity structure
350 and does not change with time. However, in the presence of local noise, the result may be biased
351 and deviate from the true value. In Fig. 12, the red line is the impedance value calculated using
352 the data observed from August 20 to August 28. The longer the data use, the more reliable the
353 result will be. The results calculated using the data observed on August 22, 23, 24, and 25 deviate
354 from the red line.

355 Moreover, Fig. 13 shows the variation in the XY component of the impedance curve calculated
356 by each hour's data at a period of 10 seconds. We use one-hour time-series data to calculate each
357 result. The impedance curve becomes more stable and correlated with the geomagnetic storm
358 event.

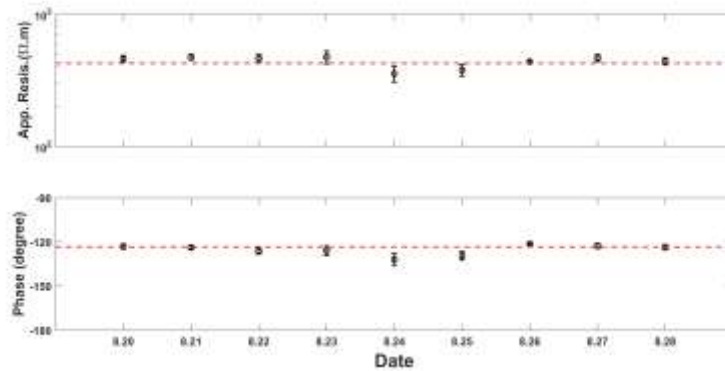
359 Fig. 11 to Fig. 13 show that the enhancement of the natural EM signal produces a more stable
360 and reliable impedance value.

361

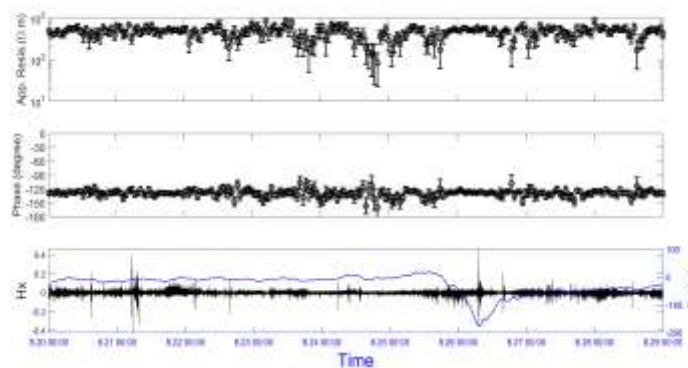


362

363 Fig. 11 The amplitude variation in periods of 16, 8, 4 and 1 seconds against the Dst index. The
 364 upper figure shows the amplitude variation from August 20 to August 28. The lowest figure
 365 shows the time variation of the Hx component along with the Dst index variation. The unit of Hx
 366 is nT. The horizontal axis denotes the time.
 367



368
 369 Fig. 12 The XY component of the impedance curve was calculated by each day's data at a period
 370 of 10 seconds. The horizontal axis denotes the date. The upper figures show the apparent
 371 resistivity, and the lower figures show the impedance phase. The red lines show the apparent
 372 resistivity and phase calculated by the data from August 20 to August 28.
 373

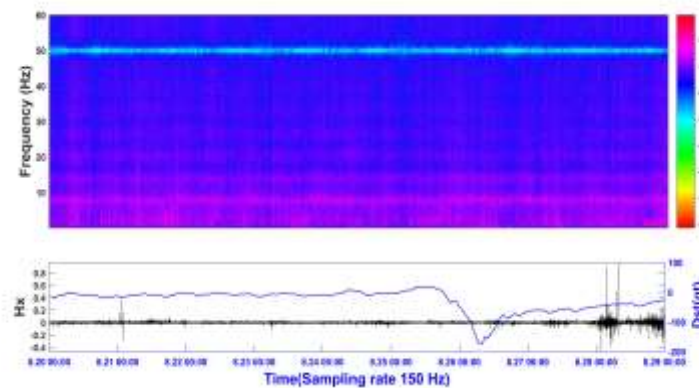


374
 375 Fig. 13 The time variation of the impedance curves calculated using each hour's time-series data
 376 at a period of 10 seconds. The horizontal axis denotes the time. One result was calculated using
 377 one-hour data. The unit of Hx is nT.

378

379 Fig. 14 shows the time-frequency distribution against the Dst index. The sampling rate is 150
380 Hz, and the content is the same, as shown in Fig. 9. There were no obvious changes in the
381 intensity that were correlated with the storms in this figure. The signal strength is extremely low
382 at 50 Hz, as it is filtered out when fieldwork is carried out. On the other hand, distinct peaks
383 appeared at approximately 7.83, 14.3, 20.8 and 27.3 Hz. These frequencies correspond to the
384 frequencies of Schumann's resonances (SRs). SR is a set of spectrum peaks in the extremely low
385 frequency (ELF) of the Earth's EM field spectrum. Lightning discharges generate global EM
386 resonances in the cavity formed by the Earth's surface and the ionosphere.

387



388

389 Fig. 14 The time-frequency distribution against the Dst index. The sampling rate is 150 Hz. The
390 content is the same as Fig. 9.

391

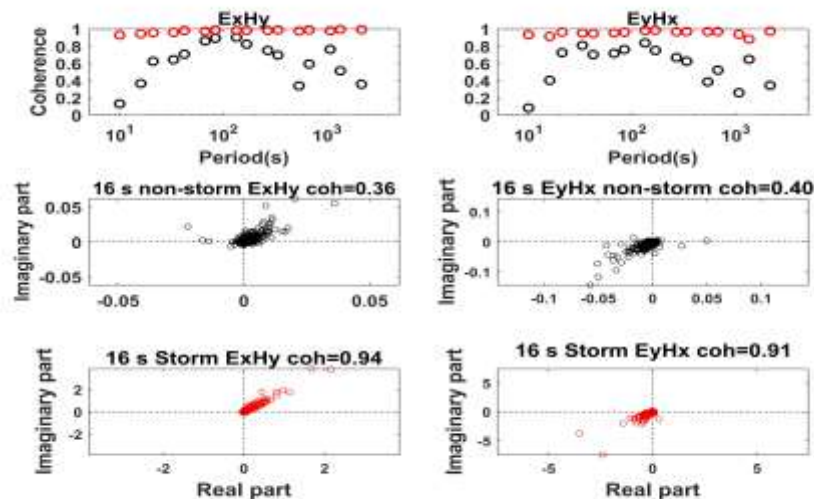
392 **4.2 Case Study 2: USArray, USA**

393 In the second case study, long-period 5-component MT time-series data observed at two sites
394 (ALW48 and TNV48) were used. The data sets were recorded with a 1-second sampling period
395 for around two weeks in 2015 from the USArray project. The geomagnetic storm occurred
396 between June 22 and June 24.

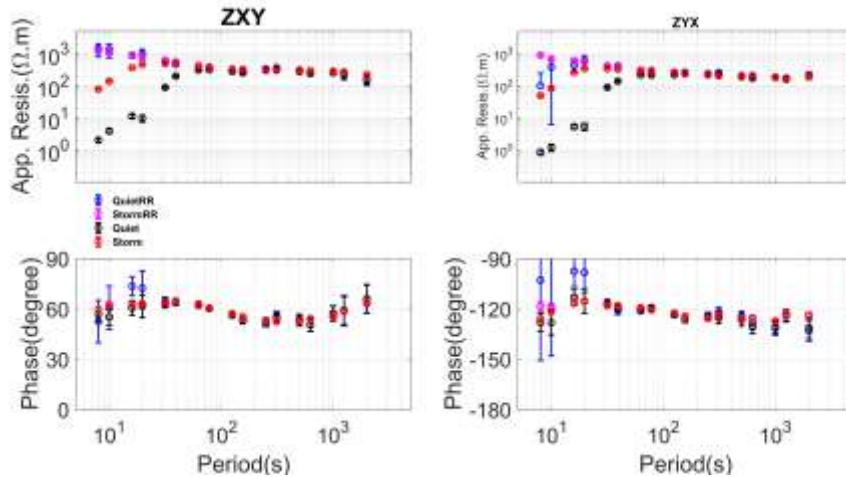
397 Fig.15 shows the distribution of coherency in different periods and cross-power spectra at 16-

398 second during the storm and non-storm days. The ordinary coherency increased from 4 to 40-
 399 second and 400 to 2,000-second during the geomagnetic storm. The low coherency during the
 400 non-storm day may be attributed to the local random noise. We can see the signal strength
 401 increased dramatically from the distribution of cross-power spectra. The preferred direction of PD
 402 between the orthogonal electric and magnetic field becomes more obvious at 16-second.

403 Fig. 15 compared four results calculated using the data observed at site TNV48 and using
 404 ALW48 as the remote reference site. The apparent resistivity of Quiet in the period from 8 to 30-
 405 second is severely down-biased. And the phase of Quiet is scattered from 8 to 30-second and 400
 406 to 2,000-second. The result calculated using the storm data is much stable than the result
 407 calculated using the non-storm data. After comparing all results, the StormRR is the most reliable,
 408 and we regard it as the true model here. The Storm result is closer to the true model than the
 409 Quiet result between 4 to 30-second. We can see from the case study that the signal strength
 410 increased during the geomagnetic storms, and a more reliable impedance is obtained using the
 411 storm data.



412
 413 Fig.15 The distribution of coherency in different periods and cross-power spectra at 16-second
 414 during the storm and non-storm days. The black color denotes the result using the non-storm data,
 415 and the red color denotes the result using the storm data.



416

417 Fig.16 The MT sounding curves using the data observed during storm day and non-storm day.

418 The Quiet result is drawn in black; the QuietRR result is drawn in blue; the Storm result is drawn

419 in red; the StormRR result is drawn in purple.

420

421 4.3 Case Study 3: KAP03, South Africa

422 In the third case study, the long-period 5-component MT time-series data observed at Kaapvaal

423 2003 (KAP03) were used. The data were recorded with a 5-second sampling period for almost a

424 month at each site using GSC LIMS systems in 2003 as a part of the SAMTEX project. The 26

425 long-period sites distributed in a NE-SW profile are shown in the right corner of Fig. 7. Data for

426 the sites located in the middle of the profile (KAP127-KAP145) were heavily contaminated by

427 DC signals from the DC train line running between Kimberley and Johannesburg (MTNET, see

428 the website in references).

429 Fig. 17 shows the time series at site 133. The sampling period is 5 seconds. In this dataset,

430 there was a geomagnetic storm event that was captured during the observation periods. The

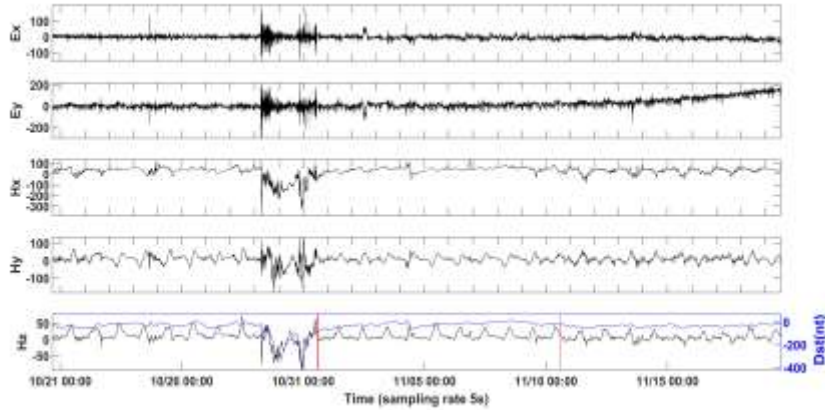
431 storms lasted approximately two days, from October 29 to October 31, 2003. We used the

432 different period time-series data of the KAP03 to analyze the geomagnetic storm's influence on

433 the impedance tensor calculation. The result calculated using the data observed at quiet site 163 is

434 shown first. Then, the data observed at noisy sites 142 and 133 are analyzed in detail. Finally, the

435 results calculated using the data observed at the other site contaminated by the heavy noise
436 between sites 130 and 145 are shown.
437



438
439 Fig. 17 Time-series of MT field data at site 133. The red vertical lines show the data gaps, and the
440 black lines show the 5-component MT data. The blue line shows the variation in the Dst index.
441 The electric field unit is mV/km, and the unit of the magnetic field is nT. The horizontal axis
442 denotes the time in UTC.

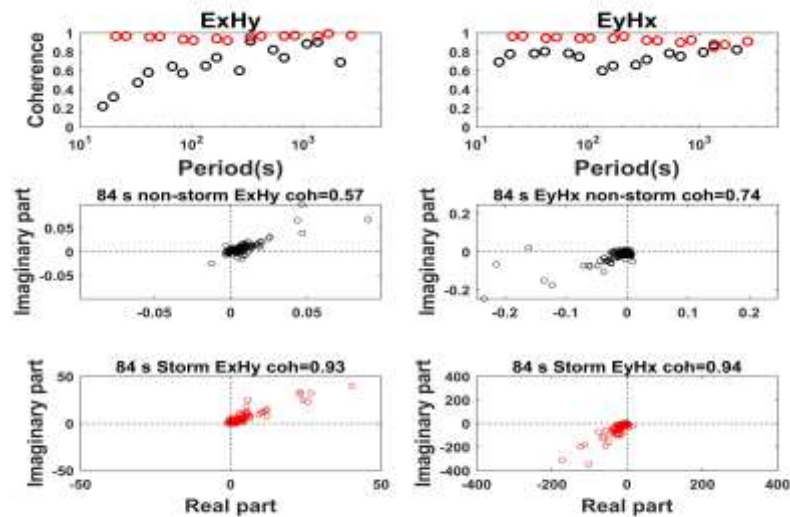
443
444 Fig. 18 shows the distribution of coherency in different periods and cross-power spectra at 84
445 seconds between storm days and non-storm days at site 163. The coherency values, i.e.,
446 $\text{Coh}(E_x, H_y)$ and $\text{Coh}(E_y, H_x)$, increased and were close to one across all periods. The preferred
447 direction of the phase difference between the orthogonal electric and magnetic fields is almost the
448 same at 84 seconds.

449 Fig. 19 shows the MT sounding curves calculated using the storm and non-storm days data at
450 site 163. The results obtained below 20 seconds are not stable. To obtain an accurate complex
451 coefficient from the time series. It is better to sample 4 points in one period. The sampling rate is
452 5 seconds. This instability may be caused by aliasing. The results calculated by EMT and BIRRP
453 using the storm and non-storm days data coincide well. From the results, we can see that the data

454 obtained during the geomagnetic storm also follows the plan-wave assumption in this area, and
 455 nonstationarity is not a problem for the method based on the FFT. It will not bias the MT transfer
 456 function.

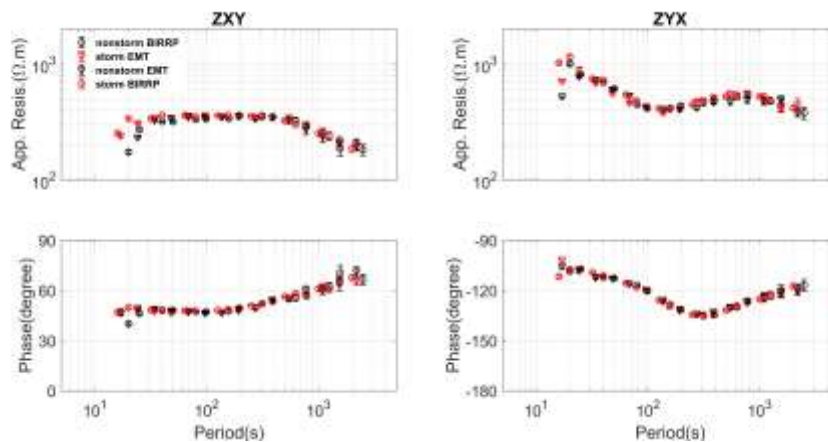
457

458



459

460 Fig. 18 The distribution of coherency in different periods and cross-power spectra at 84 seconds
 461 during the storm and non-storm days at site 163.



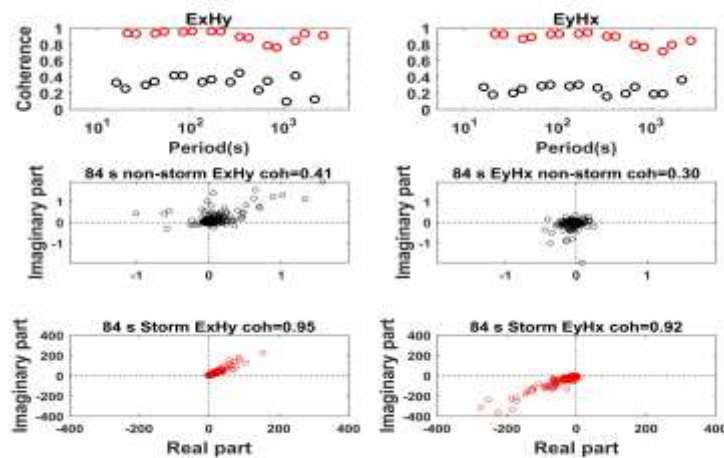
462

463 Fig. 19 The MT sounding curves calculated using the data observed during the storm and non-
 464 storm days at site 163. The triangles denote results calculated by the EMT code; the circles denote
 465 the results calculated by the BIRRP.

466

467 Fig. 20 shows the distribution of coherency in different periods and cross-power spectra at 84
468 seconds during the storm and non-storm days at site 142. There is no preferred direction of PD
469 between the orthogonal electric and magnetic fields, and the coherency is low during the non-
470 storm days. The intensity of the cross-power spectra increased almost two orders of magnitude
471 during the storm days, and the coherency increased considerably and was close to one across all
472 periods. The low coherency during the non-storm days may be attributed to the incoherent noise,
473 as shown in this case.

474 Fig. 21 shows the MT sounding curves calculated using the data observed during the storm and
475 non-storm days at site 142. The result calculated by the storm data is smoother than the Quiet and
476 QuietRR results, and the error bar is small. The QuietRR results coincide with the Storm results,
477 but the error is larger than that of the Storm results. On the other hand, the result of Quiet is quite
478 different from the results of Storm and QuietRR. Noise biased the impedance during the non-
479 storm days. During the storm, the enhancement of the natural EM signal overcame the noise and
480 provided a reliable impedance. Comparing all the impedance results, Storm is the most reliable
481 from 20 to 7,00 seconds.

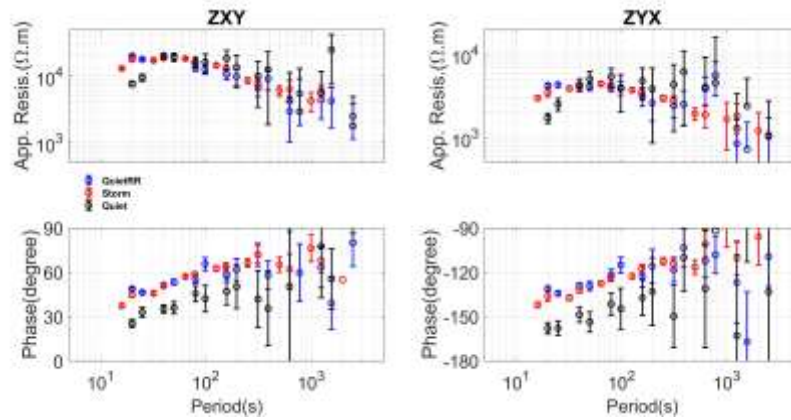


482

483 Fig. 20 The distribution of coherency in different periods and cross-power spectra at 84 seconds
484 during the storm and non-storm days at site 142. The red color denotes the result during storm

485 days. The black color denotes the result during non-storm days.

486



487

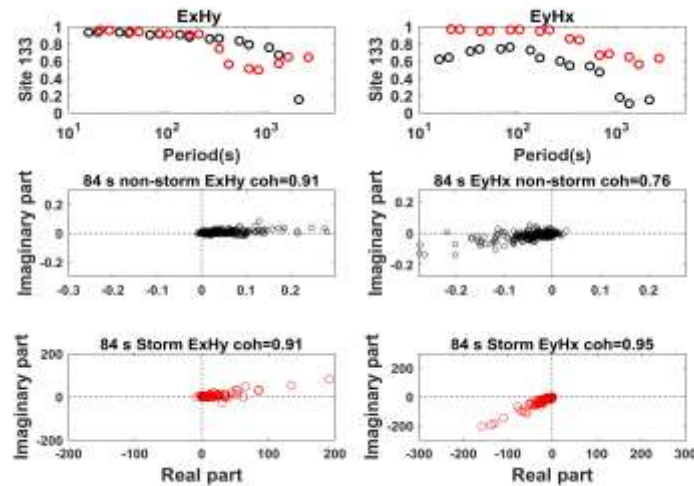
488 Fig. 21 MT sounding curves using the data observed during the storm and non-storm days at site
489 142. The Storm result is in red. The Quiet result is shown in black. The QuietRR result is shown
490 in blue.

491

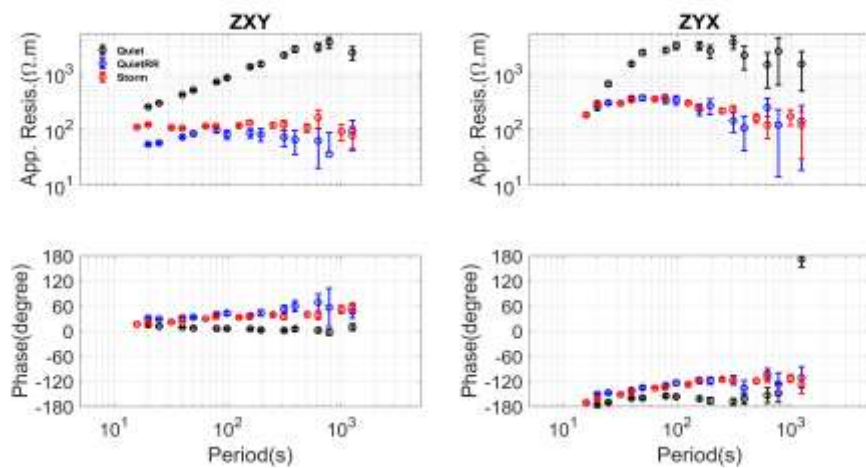
492 Fig. 22 shows the distribution of coherency across different periods and the cross-power
493 spectra at 84 seconds during the storm and non-storm days at site 133. The values of $\text{Coh}(E_x, H_y)$
494 and $\text{Coh}(E_y, H_x)$ are high during the non-storm period. However, the preferred direction of PD is
495 close to 0° and -180°. The coherent noise may have caused this phenomenon. Coherent noise
496 often appears as a spike or convex-like noise occurring simultaneously in the time domain
497 between different channels. The phase difference tends to 0° and -180°. The preferred direction of
498 PD is changed during storm days.

499 Fig. 23 shows the MT sounding curve calculated using the data observed at site 133. The XY
500 phase calculated by non-storm data is close to 0°, and the apparent resistivity increases as a line
501 on the log scale. That is the phenomenon of local noise (Zonge and Hughes, 1987). 180° or 0°
502 would correspond to a dipole electric source, which could be the train line. The impedance
503 changed using geomagnetic storm data. This result coincides with the preferred direction of PD
504 changed at 84 seconds in Fig. 22. The QuietRR result calculated using seven days of data (see

505 Table 1) coincides with the Storm result but is slightly different in the XY component between 20
 506 and 40 seconds. The remote reference technique can only reduce the influence of local noise.
 507 From Fig. 8, the signal strength during this storm is almost 50 times stronger than that during the
 508 non-storm days. The noise can be neglected in this condition. We believe that the Storm result is
 509 more reliable.



510
 511 Fig. 22 The distribution of coherency across different periods and cross-power spectra at 84
 512 seconds during the storm and non-storm days at site 133. The contents have the same meaning as
 513 those in Fig. 20.



514
 515 Fig. 23 MT sounding curves using the data observed during the storm and non-storm days at site
 516 133. The contents have the same meaning as those in Fig. 21.

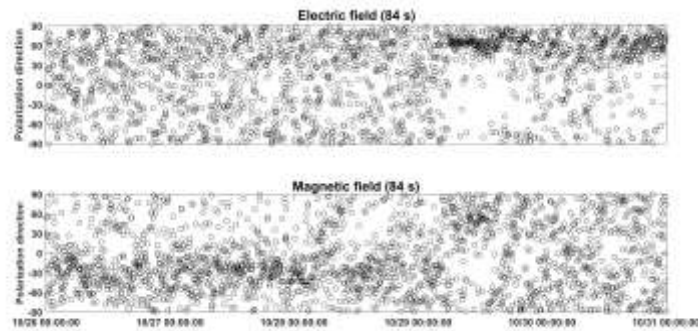
517

518 In this section, three parameters (polarization direction, RLcoh and R_AR) are used to analyze
519 the data observed at site 133. Fig. 24 shows the variation in the polarization direction at 84
520 seconds from October 26 to October 31. The magnetic field polarization has a preferred direction
521 at approximately -30° during non-storm days (October 26 to October 29) and becomes scattered
522 during geomagnetic storm days (October 29 to October 31). On the other hand, the electric field
523 polarization direction is scattered during non-storm days and has a preferred direction of
524 approximately 60° during geomagnetic storms. The polarization direction is a function of the
525 amplitude ratio and PD. The local EM noise source usually has a constant location; the incident
526 direction and the energy exhibit similar properties over time. Contrary to the natural EM signal,
527 the incident direction and power change with time. If there is a preferred polarization direction for
528 the magnetic field, we can consider that the local environment contaminates the data in that
529 period. That coincides with the high $\text{Coh}(E_x, H_y)$ and $\text{Coh}(E_y, H_x)$ and the preferred direction of
530 PD is close to 0° and -180° during the non-storm period. The data are dominated by coherent
531 noise during non-storm days.

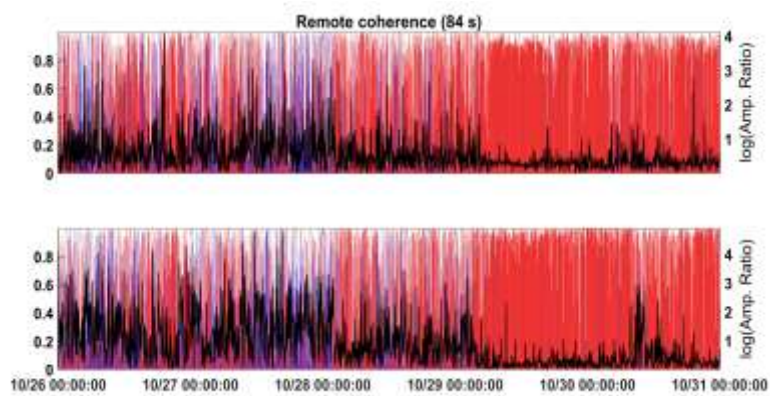
532 Fig. 25 shows the variation in RLcoh and R_AR at 84 seconds. The data observed at site 151
533 are relatively quiet and are used as remote reference data. The blue and the red line denotes the
534 RLcoh. The blue color denotes a negative value, and the red color denotes a positive value. The
535 black curve denotes the log value of R_AR.

536 The natural magnetic signal (H^{MT} and H_r^{MT}) comes from the same source and should be similar.
537 When the portion of the natural magnetic signal (H^{MT} and H_r^{MT}) is high in the local and remote
538 sites; the PD will be close to 0° ; therefore, RLcoh should be close to 1, and R_AR should be
539 stable and close to 1. Because the natural signal is weak and easily influenced by local noise
540 during non-storm days, RLcoh is scattered and low; R_AR is scattered and high during non-storm
541 days. The natural magnetic signal portion increased drastically during the geomagnetic storm, the

542 variation in RLcoh and R_AR became stable. This result indicates that the SNR is low during
 543 non-storm days and becomes high during storm days.
 544



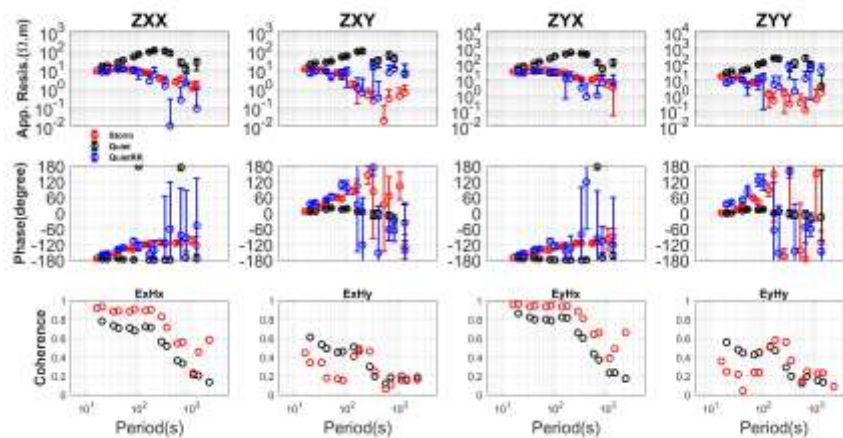
545
 546 Fig. 24 The variation in polarization direction at 84 seconds using the data observed at site 133
 547 from October 26 to October 31. The upper figure shows the polarization directions for the electric
 548 field, and the lower figure shows the polarization directions for the magnetic field.



549
 550 Fig. 25 The variation in RLcoh versus R_AR at 84 seconds using the data observed at site 133
 551 from October 26 to October 31. The blue and the red line denotes the RLcoh. Blue indicates a
 552 negative value, and red indicates a positive value. The black curve denotes the log value of R_AR.
 553

554 Fig. 26 shows the MT sounding curve and coherency distribution using the data observed
 555 during the storm and non-storm days at site 130. The $Coh(E_x, H_x)$ and $Coh(E_y, H_x)$ values are high
 556 between 10 and 200 seconds during the non-storm days; the XX and YX phases calculated by

557 non-storm data are close to 0° , and the apparent resistivity increases as a line on the log scale
 558 between 10 and 200 seconds. A similar situation occurs at site 133. We consider that the data are
 559 dominated by strong coherent noise during non-storm days. The $\text{Coh}(E_x, H_x)$ value is high while
 560 the $\text{Coh}(E_x, H_y)$ value is low during storm days; this can be interpreted as the phenomenon of
 561 PROQ. The QuietRR result using four-day data (see Table 1) coincides with the Storm result;
 562 moreover, the Storm result is smoother, and the error bar is smaller than that of the QuietRR
 563 result.
 564



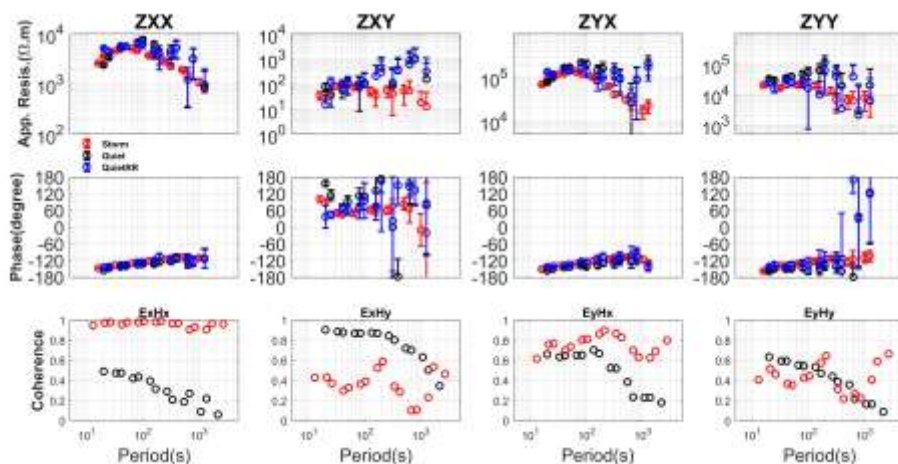
565
 566 Fig. 26 The MT sounding curves and coherency distributions obtained using the data observed
 567 during storm days and non-storm days at site 130. The storm result is shown in red. The quiet
 568 result is shown in black. The QuietRR result is shown in blue. For coherency, the red color
 569 denotes the result during storm days. The black color denotes the results obtained during non-
 570 storm days.

571
 572 Fig. 27 shows the MT sounding curve and coherency distribution using the data observed
 573 during the storm and non-storm days at site 136. $\text{Coh}(E_x, H_y)$ is relatively high between 10 and
 574 1000 seconds during the non-storm data; Fig. 28 shows the distribution of cross-power spectra of
 575 the $E_x H_x$ and $E_x H_y$ components at 168 seconds during the storm and non-storm days. The

576 preferred direction of PD between E_x and H_y is close to 0° . We consider that the strong coherent
 577 noise caused this phenomenon.

578 On the other hand, $\text{Coh}(E_x, H_x)$ is high, while $\text{Coh}(E_x, H_y)$ is low during the storm day. That can
 579 be explained as the phenomenon of PROQ. The QuietRR result using four days of data (see Table
 580 1) partially coincides with the Storm result. Moreover, the Storm result is smoother, and the error
 581 bar is smaller.

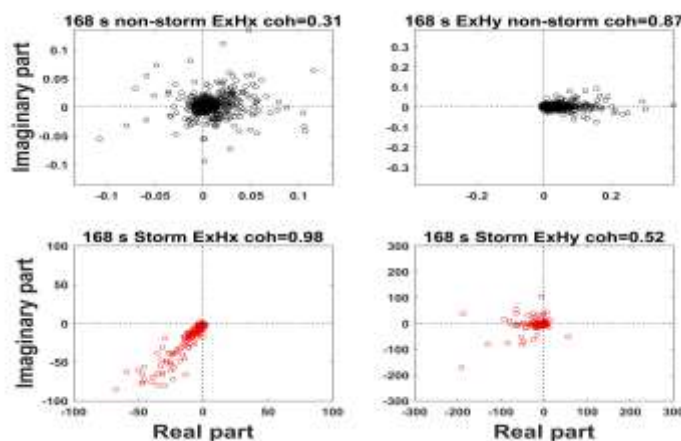
582



583

584 Fig. 27 The MT sounding curves and coherency distribution using the data observed during the
 585 storm and non-storm days at site 136. The colors have the same meanings as those in Fig. 26.

586



587

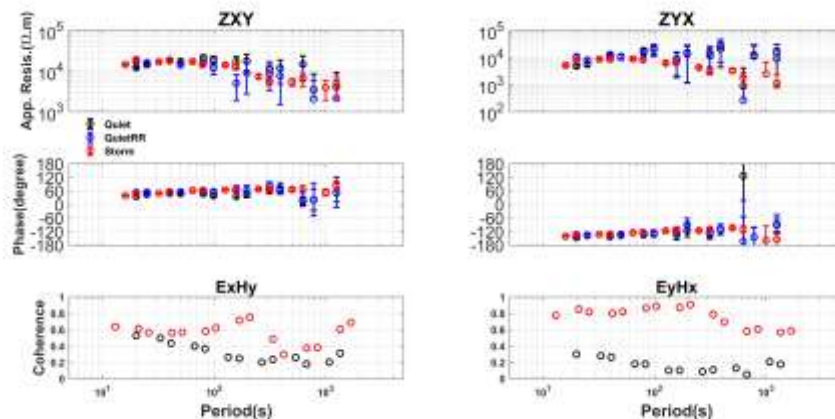
588 Fig. 28 Distribution of cross-power spectra of $E_x H_x$ and $E_x H_y$ components at 168 seconds between

589 the storm day and non-storm day at site 136. The colors have the same meanings as those in Fig.
590 20.

591

592 Fig. 29 and Fig. 30 show the MT sounding curve and coherency distribution using the data
593 observed during the storm and non-storm days at sites 139 and 145, respectively. Both the
594 coherency between the orthogonal electric and magnetic fields increased during the storm days.
595 The result calculated by the data observed on the storm day is smoother; the XY component of
596 the QuietRR result has a similar trend to the Storm result. However, the YX component is very
597 different between the QuietRR and Storm results at both sites. It is difficult to distinguish which
598 represents the real conditions. From the perspective of SNR and based on the analysis in the
599 previous case study, the storm has a positive effect on the MT data quality; we believe that the
600 Storm result is more reliable.

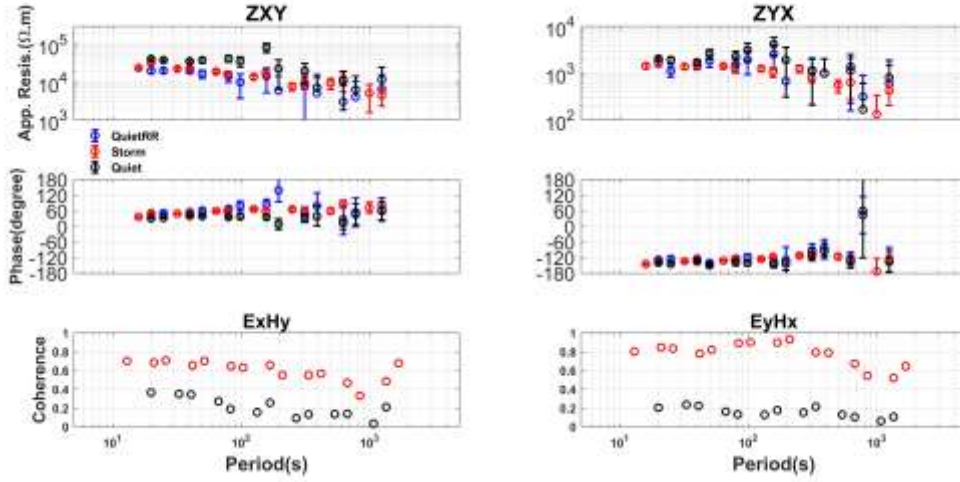
601



602

603 Fig. 29 MT sounding curves and coherency distribution using the data observed during the storm
604 and non-storm days at site 139. The colors have the same meanings as those in Fig. 26.

605



606

607 Fig. 30 MT sounding curves and coherency distribution using the data observed during the storm

608 and non-storm days at site 145. The colors have the same meanings as those in Fig. 26.

609

610 5 DISCUSSION

611 In this section, we discuss how to use multiple parameters to estimate the data quality. Coherency

612 is an important parameter to discuss the data quality. However, the characteristic of coherency is

613 different in different situations. At first, we discuss the relationship between impedance and

614 coherency. According to least-squares theory (Sims et al., 1971); Z_{xy} can be calculated as follows:

$$615 \quad Z_{xy} = \frac{\langle E_x \bar{H}_y \rangle \langle H_x \bar{H}_x \rangle - \langle E_x \bar{H}_x \rangle \langle H_x \bar{H}_y \rangle}{\langle H_y \bar{H}_y \rangle \langle H_x \bar{H}_x \rangle - \langle H_y \bar{H}_x \rangle \langle H_x \bar{H}_y \rangle} = \frac{C - D}{E - F} \quad (14)$$

616 For the denominator, there is a relationship between the coherency as follows:

$$617 \quad |C| = |\langle E_x \bar{H}_y \rangle \langle H_x \bar{H}_x \rangle| = \text{coh}(E_x, H_y) \sqrt{\langle E_x \bar{E}_x \rangle \langle H_y \bar{H}_y \rangle} \langle H_x \bar{H}_x \rangle, \quad (15)$$

$$618 \quad |D| = |\langle E_x \bar{H}_x \rangle \langle H_x \bar{H}_y \rangle| = \text{coh}(E_x, H_x) \sqrt{\langle E_x \bar{E}_x \rangle \langle H_x \bar{H}_x \rangle} \text{coh}(E_x, H_x) \sqrt{\langle H_x \bar{H}_x \rangle \langle H_y \bar{H}_y \rangle}, \quad (16)$$

$$619 \quad \frac{|C|}{|D|} = \frac{|\langle E_x \bar{H}_y \rangle \langle H_x \bar{H}_x \rangle|}{|\langle E_x \bar{H}_x \rangle \langle H_x \bar{H}_y \rangle|} = \frac{\text{coh}(E_x, H_y)}{\text{coh}(E_x, H_x) \text{coh}(H_x, H_y)}, \quad (17)$$

620 For the denominator part of equation 14, there is a relationship as follows:

$$621 \quad |E| = |\langle H_x \bar{H}_x \rangle \langle H_y \bar{H}_y \rangle| \quad (18)$$

$$622 \quad |F| = |\langle H_y \bar{H}_x \rangle \langle H_x \bar{H}_y \rangle| = \text{coh}^2(H_x, H_y) \langle H_x \bar{H}_x \rangle \langle H_y \bar{H}_y \rangle \quad (19)$$

623
$$\frac{|E|}{|F|} = \frac{1}{\text{coh}^2(H_x, H_y)} \quad (20)$$

624 Because various sources generate natural magnetic signals, they generate magnetic fields that
625 vary in their incident directions, which means H_x and H_y are not coherent, and $\text{Coh}(H_x, H_y)$ is a
626 small value. In the condition that the $\text{Coh}(E_x, H_y)$ is relatively high while the $\text{Coh}(E_x, H_x)$ is small.
627 The numerator of Eq. 14 will be dominant by the C part. The denominator is dominant by the E
628 part.

629 The Z_{xy} can be rewritten as follows:

630
$$Z_{xy} = \frac{\langle E_x H_y^\dagger \rangle}{\langle H_y H_y^\dagger \rangle}. \quad (21)$$

631 In this situation, Z_{xy} is determined by the orthogonal component of the electric and magnetic field.
632 A similar analysis to Z_{xx} , Z_{xx} is undeterminable. When $\text{Coh}(E_x, H_y)$ is relatively high while
633 $\text{Coh}(E_x, H_x)$ is small; the field data can be explained as the 1-D and 2-D cases. Here we also need
634 to quantify the coherency value in the different geological environments by doing some
635 simulation. For example, rotate the observation axes in the 2-D case by the step of 5° , how high
636 the coherency will be. We can see the example at TNV 48 from USArray, site 142 from KAP03.
637 The coherency between the orthogonal magnetic and electric components is relatively low during
638 the non-storm day and increased dramatically during the strong storm. The low coherency can be
639 attributed to the incoherent noise in this case.

640 On the contrary that the coherency between the orthogonal component $\text{Coh}(E_x, H_y)$ is relatively
641 low while the $\text{Coh}(E_x, H_x)$ is high. The Z_{xy} is undeterminable and Z_{xx} is determinable. The
642 phenomenon of PROQ appears. In this situation, we cannot explain the data by the 1-D or 2-D
643 case. We can see the example at Sawauchi station, sites 130 and 136 from KAP03. Both site 130
644 and 136 is contaminated by coherent noise, and the $\text{Coh}(E_x, H_y)$ become low while the $\text{Coh}(E_x, H_x)$
645 become relatively high during the storm day.

646 The coherent noise may have a high coherency value and appear as the spike, or convex-like,

647 or other kinds of noise in the time domain at the different channel simultaneously. And the phase
648 difference between the two-channel tends to 0° or 180° . It is better to check the phase by plot the
649 distribution of the cross-power spectra. To estimate the data quality precisely, we would better
650 combine other parameters to discuss the situation.

651 The polarization direction is a function of PD and AR between the two orthogonal fields. The
652 local EM noise source usually has a constant location; the incident direction and the energy have
653 a similar property along with time. Contrary to the natural EM signal, the incident direction and
654 power are changed with time. If there is a preferred polarization direction for the magnetic field,
655 we can consider that the data is contaminated by coherent noise in that period. This situation can
656 be seen at site 133. But sometimes, the data is contaminated by incoherent noise. There is no
657 preferred polarization direction for the magnetic field. This situation appears in site 142 but is not
658 shown in this paper.

659 Suppose there is a quiet remote reference site. We also could use the RLcoh and R_AR to
660 measure the similarity between the local and remote sites to evaluate the influence of noise. This
661 example is shown in the data analysis at site 133.

662 Finally, the most important parameter to discuss the data quality is the result impedance. The
663 sounding curve should be smooth according to the forwarding modeling. On the other hand, in
664 the influence of strong locale noise, the phase will be close to 0° or 180° , and the apparent
665 resistivity increases as a line in the log scale (Zonge and Hughes, 1987); this phenomenon appear
666 during the non-storm day at site 130 and 133. Because the remote reference technique can
667 suppress the local noise, and the remote reference result can be used as a standard to evaluate the
668 data quality. The examples are shown in sites 130,136,139,145 from KAP03 and TNV48 from
669 USArray. Until now, we discussed how to use multiple parameters to estimate the geomagnetic
670 storm on the data quality. All examples of the method can be found in the case studies.

671 Finally, we will discuss the source effect and nonstationarity of the data observed during the
672 storm day. At mid-latitudes, geomagnetic pulsations (Pc's) in the Pc3-4 band ($\sim 10 - 100$ s)

673 associated with field-line resonances can violate the fundamental assumption of the MT method
674 over the resistive regions; where skin depths are large (Murphy and Egbert, 2018). In this case,
675 the source effect is inevitable and is place-dependent. In this paper, from the perspective of SNR,
676 we demonstrate the positive effect of a geomagnetic storm on the MT data quality, the impedance
677 calculated using the data observed during the geomagnetic storm and the non-storm day at the
678 quiet site 163 and Sawauchi station coincide well. It shows that the signal holds the plane-wave
679 assumption, and the nonstationarity is not a problem for the method based on the FFT in this area.
680 Otherwise, the result calculated by the storm period data should be biased. The sources effect may
681 be considered near the auroral or equatorial electrojets. But the plane wave assumption is
682 generally acceptable at midlatitudes.

683

684 **6 CONCLUSIONS**

685 It is well known that the signal strength will increase during a geomagnetic storm in the MT
686 community. Still, the demonstration that shows the positive effects on the MT impedance by the
687 field data is rare. This paper showed the positive influence of the geomagnetic storm on MT data
688 quality by three case studies in mid-latitude. Using the data observed during a strong geomagnetic
689 storm may overcome the influence of the local noise, depending on the strength of the
690 geomagnetic storm and local noise. We obtained a more reliable and interpretable impedance
691 using the data observed during the strong geomagnetic storm to calculate the impedance in the
692 survey line from Kap03, which is contaminated by the strong noise.

693 MT field data include natural signal sources and noise. Along with urban constructions,
694 artificial disturbances to EM observations are becoming more and more serious. The observation
695 occasionally contains continuous noise, which is difficult to get a reliable result from the current
696 technique. When we redo the MT campaign in the noisy site, we may get a reliable result using
697 the data observed during geomagnetic storms. Sometimes, the variation during storm periods can
698 be 100 times greater than in the non-storm period data. In that condition, the noise can be

699 neglected. However, a strong geomagnetic storm doesn't occur frequently. It is possible to predict
700 the geomagnetic storm by the space weather forecast information. The Space Weather Prediction
701 Center (SWPC; see the website in references) provides information about space weather in the
702 coming three days. Utilizing the data observed during the strong geomagnetic storm may bring a
703 reliable result despite the site contaminated by continuous noise.

704 To get the accurate complex coefficient from the time series, we suggest that it is better to
705 contain at least four times longer than the expected period. For 1,000-second, a time-series
706 segment with 4,000 seconds is needed to get accurate spectra. The overlay rate is 50% to keep
707 each data's independence and get more sample data. By the continuous 4-hour time-series data,
708 we may get about eight samples to do the impedance estimation in the frequency domain by FFT.
709 If there is continuous 4-hour geomagnetic storm data, we may get a relatively reliable tensor until
710 1,000 seconds, depending on the geomagnetic storm's length. The longer the geomagnetic storm
711 last. A more stable result can be obtained. By the statistical analysis of the geomagnetic storm,
712 one year had about ten strong geomagnetic events, and about five events lasted more than 4 hours
713 on average. That is practical and meaningful for MT exploration.

714

715 **DECLARATION**

716

717 **Availability of data and materials**

718 The magnetic time-series data observed at the KAK station is downloaded from the
719 INTERMAGNET (International Real-time Magnetic Observatory Network). The SAMTEX team
720 and USArray team provided the long period time-series data to investigate. Kap03 data can be
721 download from MTNET (see the reference). USArray data can be download from IRIS
722 (Incorporated Research Institutions for Seismology). Nittetsu Mining Consultants Co., Ltd.
723 provided the broadband frequency MT time-series data observed at Sawauchi, Japan. The Dst
724 index data can be download from the WDC for Geomagnetism, Kyoto. Alan Chave provided the

725 BIRRP code. Maik Neukirch provided the EMT code.

726

727 **Competing interests**

728 We know of no conflicts of interest associated with this publication. We declare that this
729 manuscript is original, has not been published before and is not currently being considered for
730 publication elsewhere.

731

732 **Funding**

733 'Not applicable.'

734

735 **Authors' contributions**

736 Hao Chen processed the time series data, created the result and wrote the paper. Hao Chen
737 contributes about 60%. Hideki Mizunaga reviewed the paper and contributed about 30%;
738 Toshiaki Tanaka contributed about 10% to this work.

739

740 **Acknowledgments**

741 We thank the INTERMAGNET (International Real-time Magnetic Observatory Network) for
742 providing the magnetic time-series data observed at the KAK station. We thank all SAMTEX and
743 USArray team members for providing the time-series data used in this study. We also thank
744 Nittetsu Mining Consultants Co., Ltd. for providing the broadband frequency MT time-series data
745 observed at Sawauchi, Japan. We thank the WDC for Geomagnetism, Kyoto, for providing the
746 Dst index data to do the statistical analysis of the geomagnetic storm. Finally, we express special
747 thanks to Maik Neukirch for his constructive comments to improve the manuscript. We also
748 thank Ute Weckmann, Louise Alexander, Ben Murphy, James Macnae and two anonymous
749 reviewers who reviewed and gave us constructive comments to improve the manuscript.

750

751 **REFERENCES**

- 752 Cagniard, L., 1953. The basic theory of the magneto-telluric method of geophysical prospecting.
753 *Geophysics*, **18**, 605–635.
- 754 Constable, C., 2016. Earth's electromagnetic environment. *Surv. Geophysics*, **37**, 27–45.
- 755 Constable, C. G. and Constable, S.C., 2004. Satellite magnetic field measurements: applications
756 in studying the deep Earth. *State Planet Front. Chall. Geophysics*, **19**, 147.
- 757 Chen, J., Heincke, B., Jegen, M. and Moorkamp, M. 2012. Using empirical mode decomposition
758 to process marine magnetotelluric data, *Geophys. J. Int.*, **190**, 293–309.
- 759 Chouteau, M.Tournerie, B., 2000. Analysis of magnetotelluric data showing phase rolling out of
760 quadrant (PROQ), SEG Technical Program Expanded Abstracts 2000. Society of Exploration
761 Geophysicists, pp. 344–346.
- 762 Chave, A. D. and Thomson, D. J., 2004. Bounded influence estimation of magnetotelluric
763 response functions, *Geophys. J. Int.*, **157**, 988–1006.
- 764 Chave, A.D., Jones, A.G., 2012. The magnetotelluric method: Theory and practice. Cambridge
765 University Press.
- 766 Egbert, G.D., Eisel, M., Boyd, O.S., Morrison, H.F., 2000. DC trains and Pc3s: Source effects in
767 mid - latitude geomagnetic transfer functions. *Geophys. Res. Lett.* **27**, 25 - 28.
- 768 Fowler, R.A., Kotick, B.J., Elliott, R.D., 1967. Polarization analysis of natural and artificially
769 induced geomagnetic micropulsations. *J. Geophys. Res.* **72**, 2871–2883.
- 770 Gamble, T. D., Goubau, W. M. and Clarke, J., 1979. Magnetotellurics with a remote reference,
771 *Geophysics*, **44**, 53–68.
- 772 Garcia, X., Chave, A.D., Jones, A.G., 1997. Robust processing of magnetotelluric data from the
773 auroral zone. *J. Geomagn. Geoelectr.* **49**, 1451–1468.
- 774 Garcia, X. and Jones, A. G., 2002. Atmospheric sources for audio-magnetotelluric (AMT)
775 sounding, *Geophysics*, **67**, 448-458.

776 Hennessy, L., Macnae, J., 2018. Source-dependent bias of spherics in magnetotelluric responses.
777 Geophysics 83, E161–E171.

778 Lezaeta, P., Chave, A., Jones, A.G., Evans, R., 2007. Source field effects in the auroral zone:
779 Evidence from the Slave craton (NW Canada). Phys. Earth Planet. Inter. **164**, 21–35.

780 Marple, S.L., Marino, C., 2004. Coherency in signal processing: a fundamental redefinition,
781 Conference Record of the Thirty-Eighth Asilomar Conference on Signals, Systems and
782 Computers, 2004. IEEE, pp. 1035–1038.

783 Murphy, B.S., Egbert, G.D., 2018. Source biases in midlatitude magnetotelluric transfer functions
784 due to Pc3-4 geomagnetic pulsations. Earth Planets Space **70**, 1–9.

785 McPherron, R.L., 2005. Magnetic pulsations: their sources and relation to solar wind and
786 geomagnetic activity, *Surv. Geophysics*, **26**, 545–592.

787 Mareschal, M., 1981. Source effects and the interpretation of geomagnetic sounding data at sub-
788 auroral latitudes. Geophys. J. Int. **67**, 125–136.

789 MTNET, <https://www.MTnet.info/data/kap03/kap03.html>.

790 Neukirch, M. and Garcia, X. 2014. Nonstationary magnetotelluric data processing with the
791 instantaneous parameter, *J. Geophys. Res. Solid Earth*, **119**, 1634–1654.

792 Oettinger, G., Haak, V., Larsen, J. C., 2001. Noise reduction in magnetotelluric time-series with a
793 new signal–noise separation method and its application to a field experiment in the Saxonian
794 Granulite Massif, *Geophys. J. Int*, **146**, 659–669.

795 Rikitake, T., 1948. 1. Notes on electromagnetic induction within the Earth. Bull. Earthquake Res.
796 Inst., **24**, 1-9.

797 Sims, W. E., Bostick, F. X., and Smith, H. W., 1971. The estimation of magnetotelluric impedance
798 tensor elements from measured data, *Geophysics*, **36**, 938–942.

799 Smirnov, M. Y., 2003. Magnetotelluric data processing with a robust statistical procedure having
800 a high breakdown point, *Geophys. J. Int.*, **152**, 1–7.

801 SWPC (The Space Weather Prediction Center),

802 <https://www.swpc.noaa.gov/content/wmo/geomagnetic-activity>.

803 Tikhonov, A. N., 1950. On determining electrical characteristics of the deep layers of the Earth's
804 crust, in Doklady, Citeseer, 295–297.

805 Viljanen, A., Pirjola, R., & Hákkinen, L., 1993. An attempt to reduce induction source effects at
806 high latitudes, Journal of geomagnetism and geoelectricity, **45**(9), 817-831.

807 Weckmann, U., Magunia, A. and Ritter, O., 2005. Effective noise separation for magnetotelluric
808 single site data processing using a frequency domain selection scheme, *Geophys. J. Int.*, **161**,
809 635–652.

810 Weckmann, U., Ritter, O., Haak, V., 2003. A magnetotelluric study of the Damara Belt in Namibia:
811 2. MT phases over 90 reveal the internal structure of the Waterberg Fault/Omaruru Lineament.
812 *Phys. Earth Planet. Inter.* **138**, 91–112.

813 Yu, G., Xiao, Q., Li, M., 2018. Anisotropic Model Study for the Phase Roll Out of Quadrant Data
814 in Magnetotellurics.

815 Zonge, K. L. and Hughes, L. J., 1987. Controlled source audio-frequency magnetotellurics, in
816 *Electromagnetic Methods in Applied Geophysics. Applications* (ed. Nabighian, M. N.), SEG,
817 713–809.

818

Figures

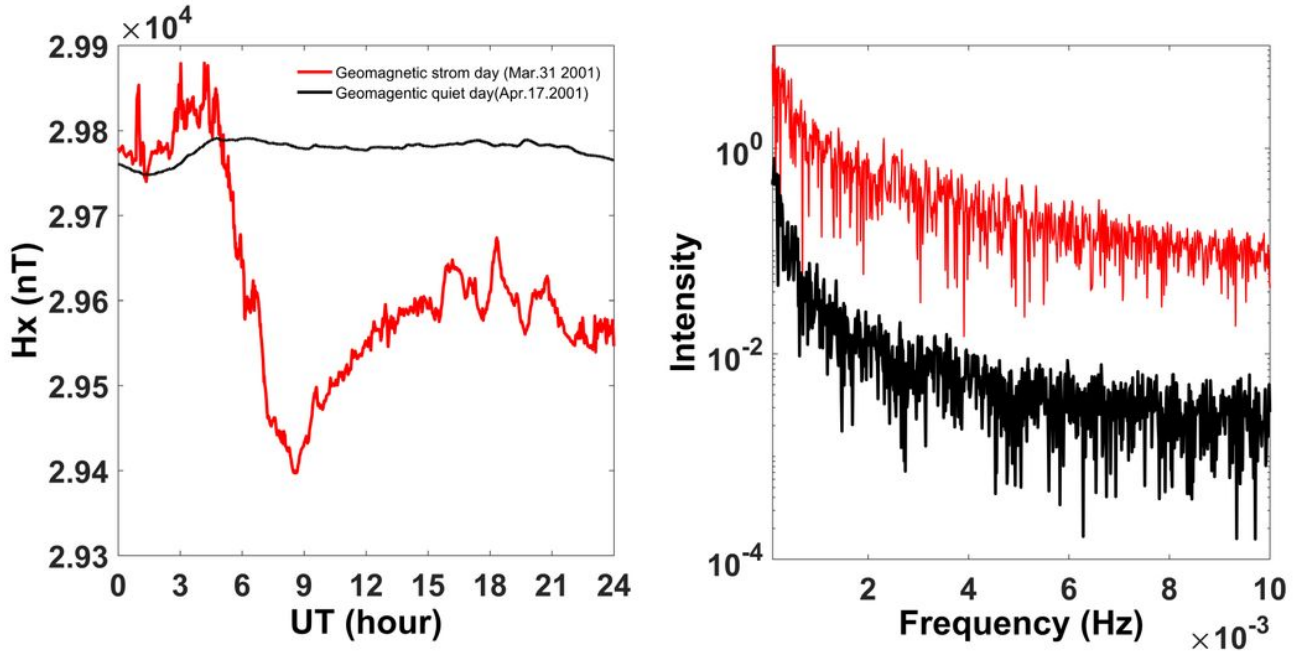


Figure 1

The geomagnetic intensities along the N-S direction during a storm day and a non-storm day. The black lines denote the non-storm day's data, and the red lines denote the storm day's data. The left is a profile in the time domain, and the right is a profile in the frequency domain.

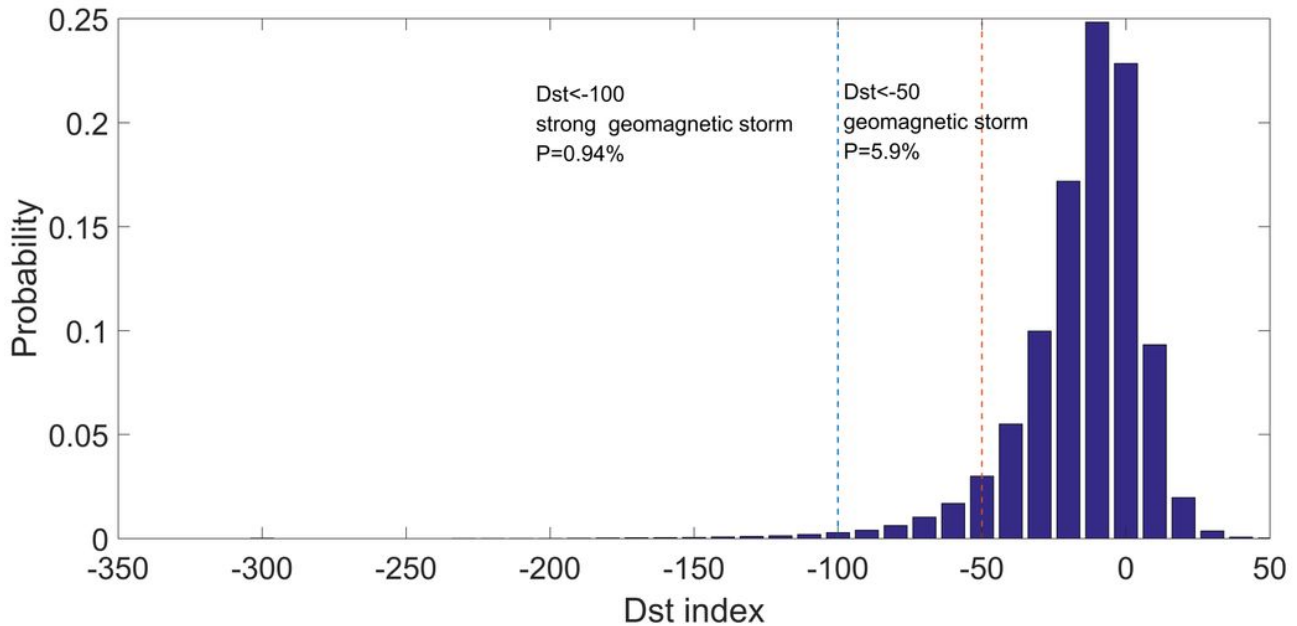


Figure 2

The distribution of strong storms based on the Dst index between 1957 - 2020, the orange line denotes Dst (≤ -50 nT), and the light blue line denotes Dst (≤ -100 nT).

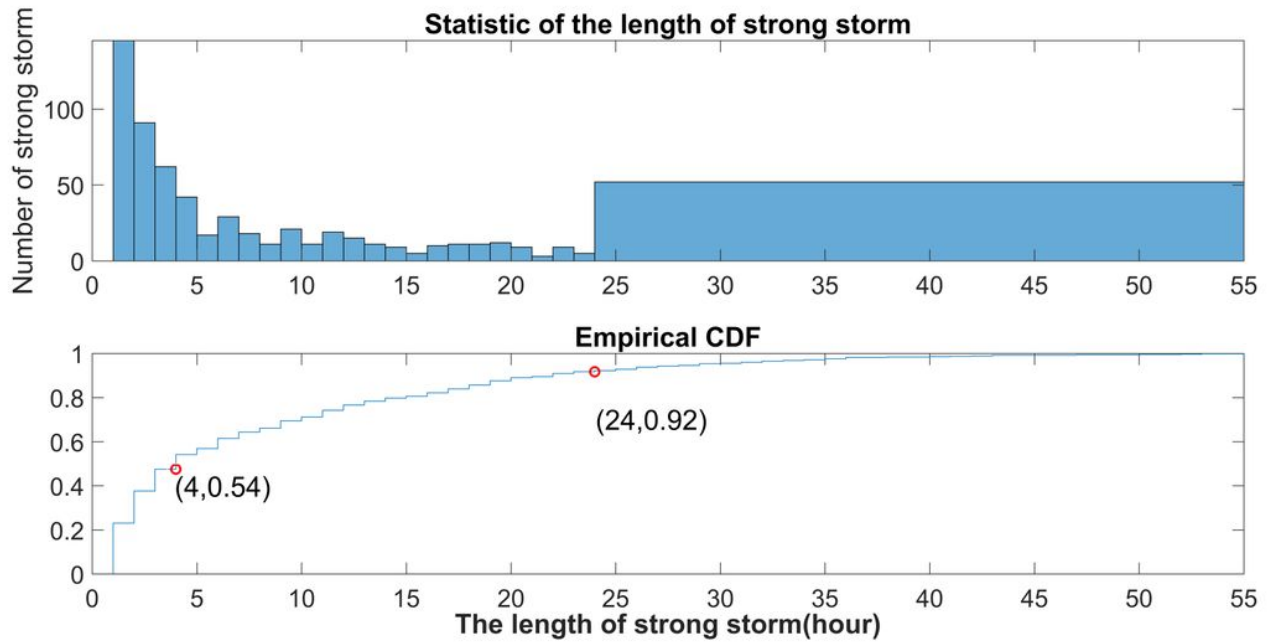


Figure 3

The statistical analysis of each strong geomagnetic storm event. The upper figure shows the number of each strong geomagnetic storm event in a different storm event length. The lower figure shows the cumulative distribution of the upper figure.

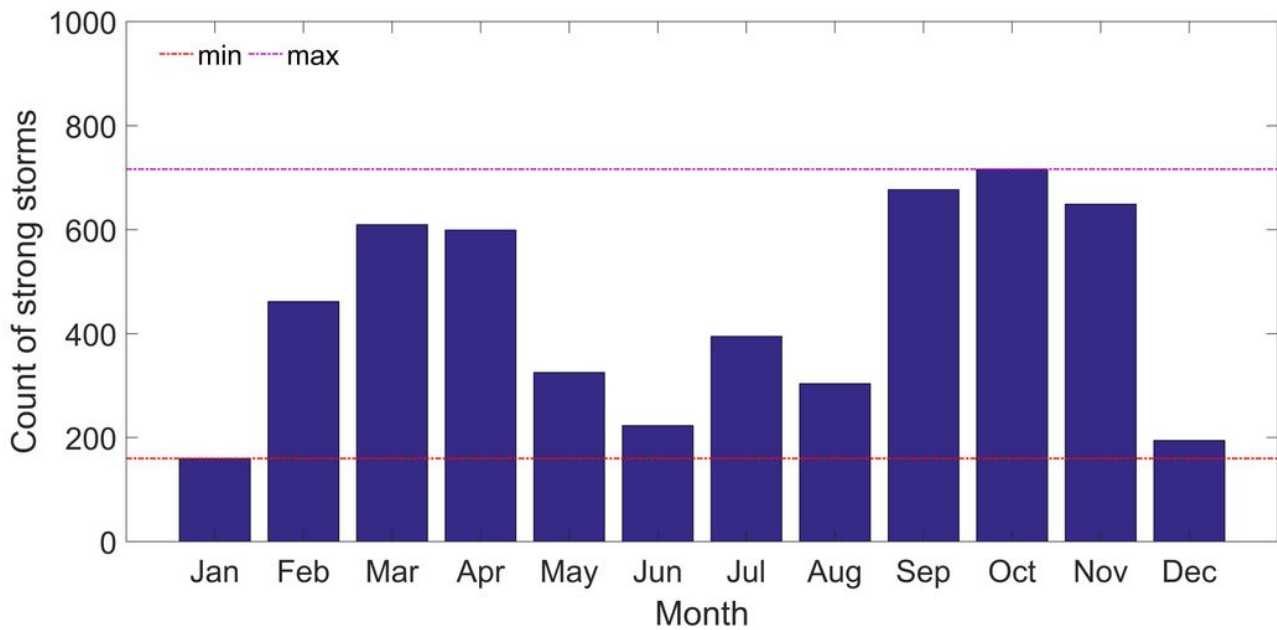


Figure 4

The monthly count of strong geomagnetic storms based on the Dst index.

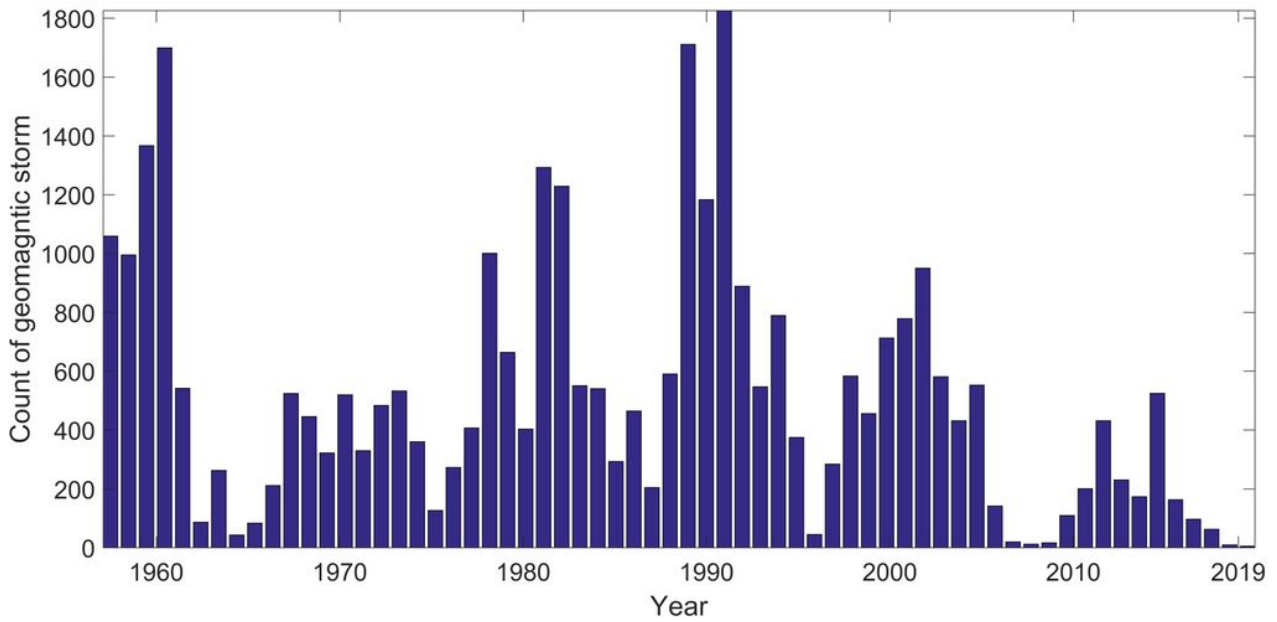


Figure 5

The yearly count of geomagnetic storms based on the Dst index from 1957 to 2020.

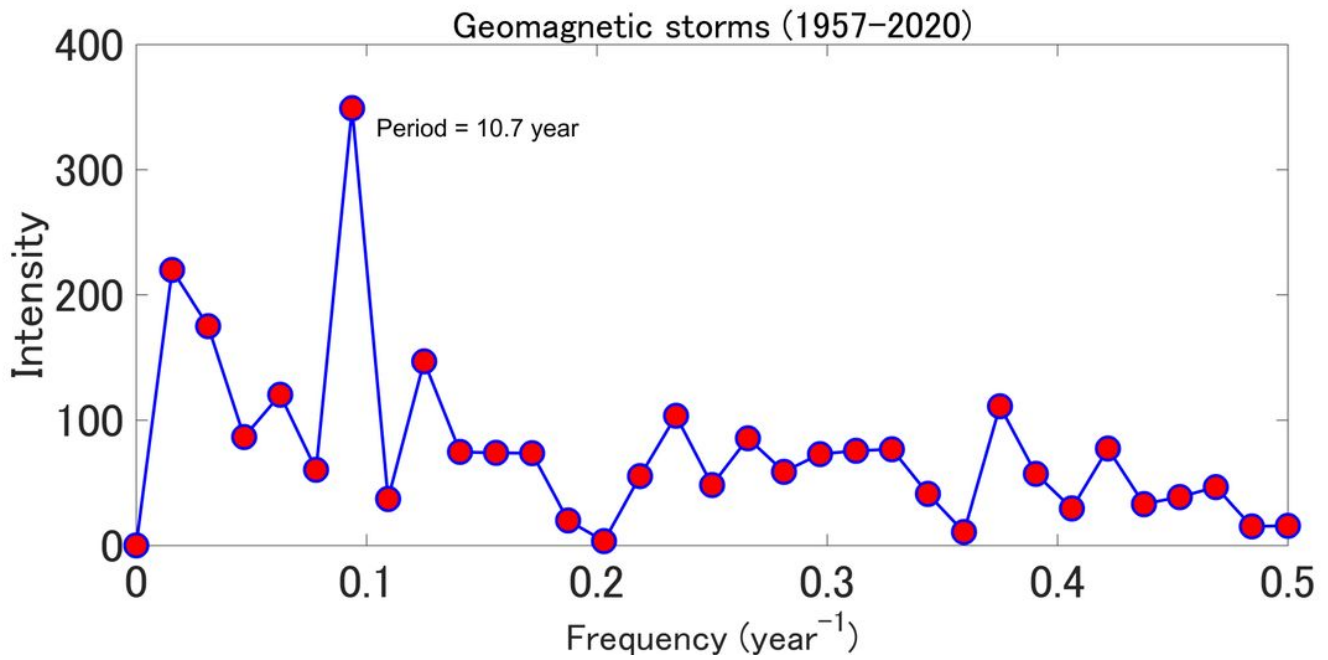


Figure 6

The calculated periods by Fourier analysis using the yearly count of geomagnetic storms from 1957 to 2020.

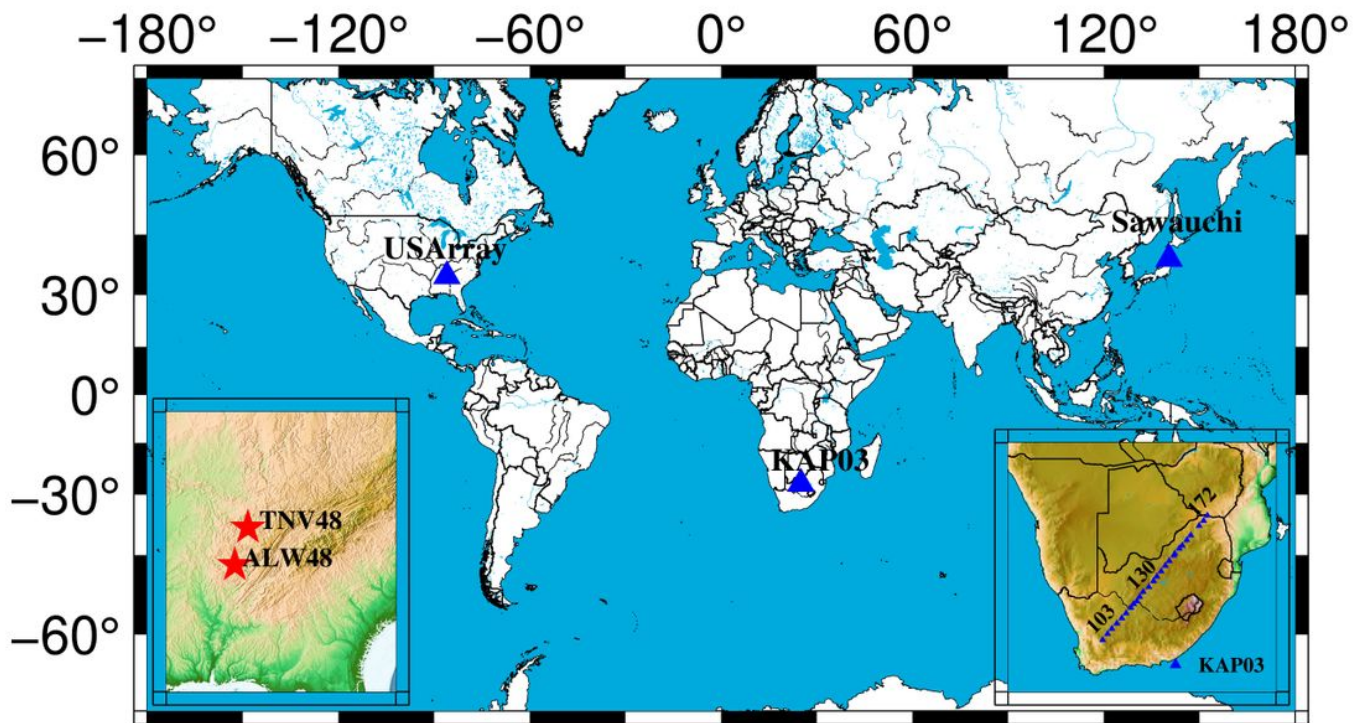


Figure 7

The location map in the three case studies (KAP03, USArray, Sawauchi). The left map shows the detailed site location used in USArray, and the right map shows the survey line of KAP03. Note: The designations employed and the presentation of the material on this map do not imply the expression of any opinion whatsoever on the part of Research Square concerning the legal status of any country, territory, city or area or of its authorities, or concerning the delimitation of its frontiers or boundaries. This map has been provided by the authors.

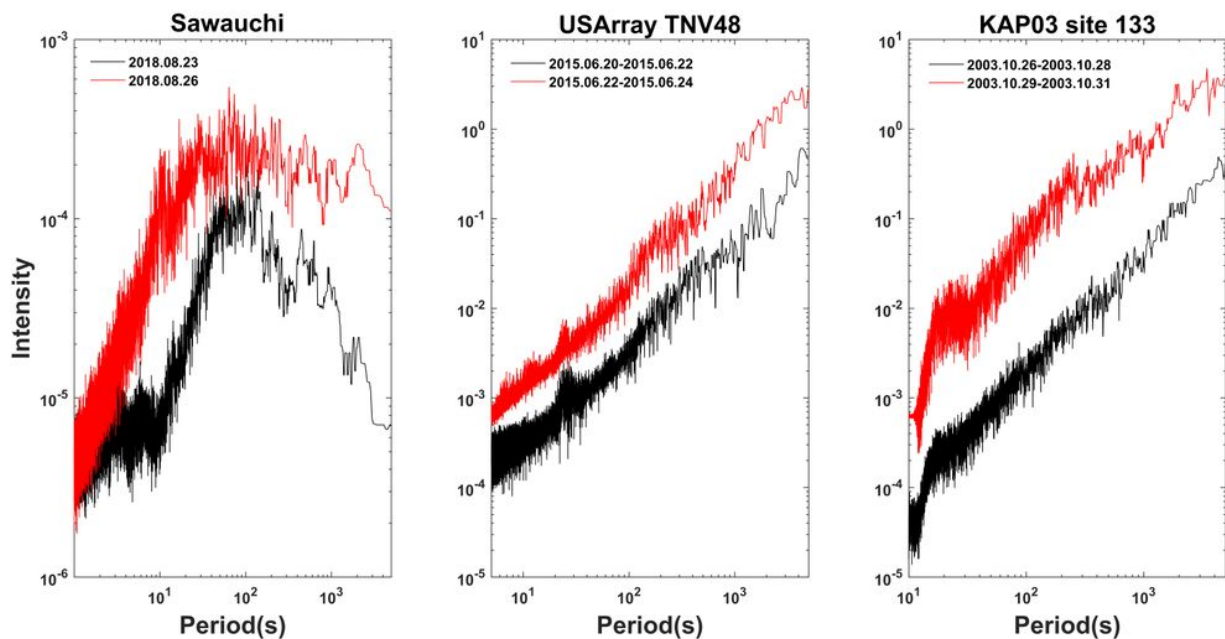


Figure 8

Comparison of the spectrum calculated by the Hx component observed during the storm and non-storm days. The black lines denote the non-storm day's data, and the red lines denote the storm day's data. The horizontal axis denotes the period. The vertical axis denotes the intensity.

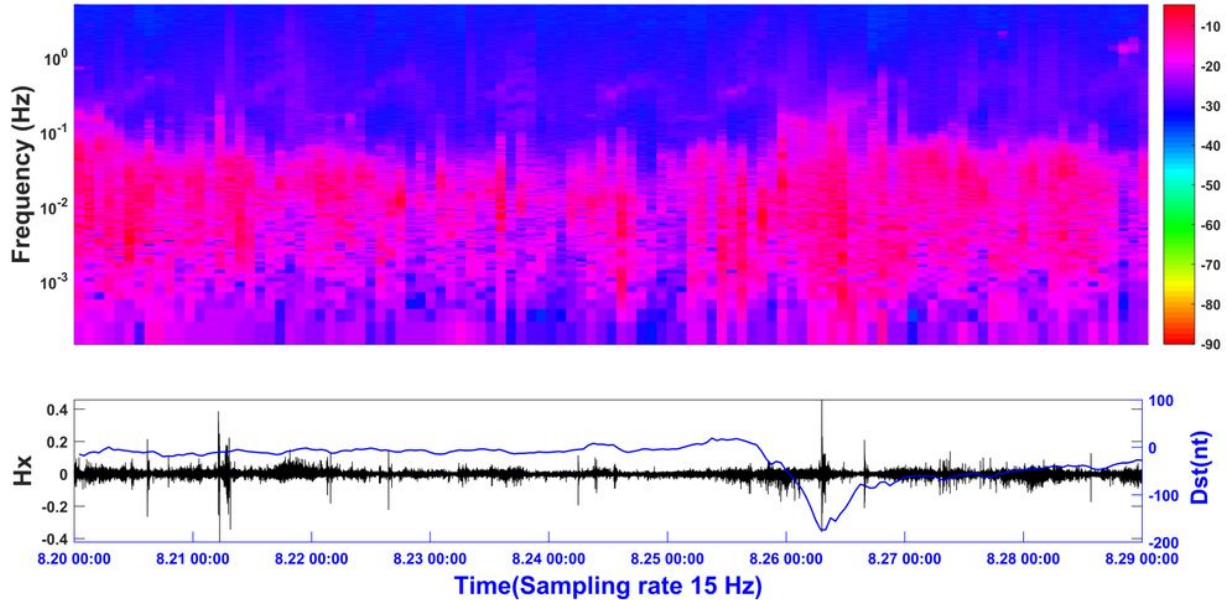


Figure 9

The time-frequency distribution against the Dst index variation and the sampling rate is 15 Hz. The upper figure shows the time-frequency distribution from August 20 to 29. The color denotes the value of $10 \cdot \log_{10}$ (amp.). The lower figure shows the time variations of the Hx component along with the Dst index. The unit of Hx is nT. The horizontal axis denotes the date.

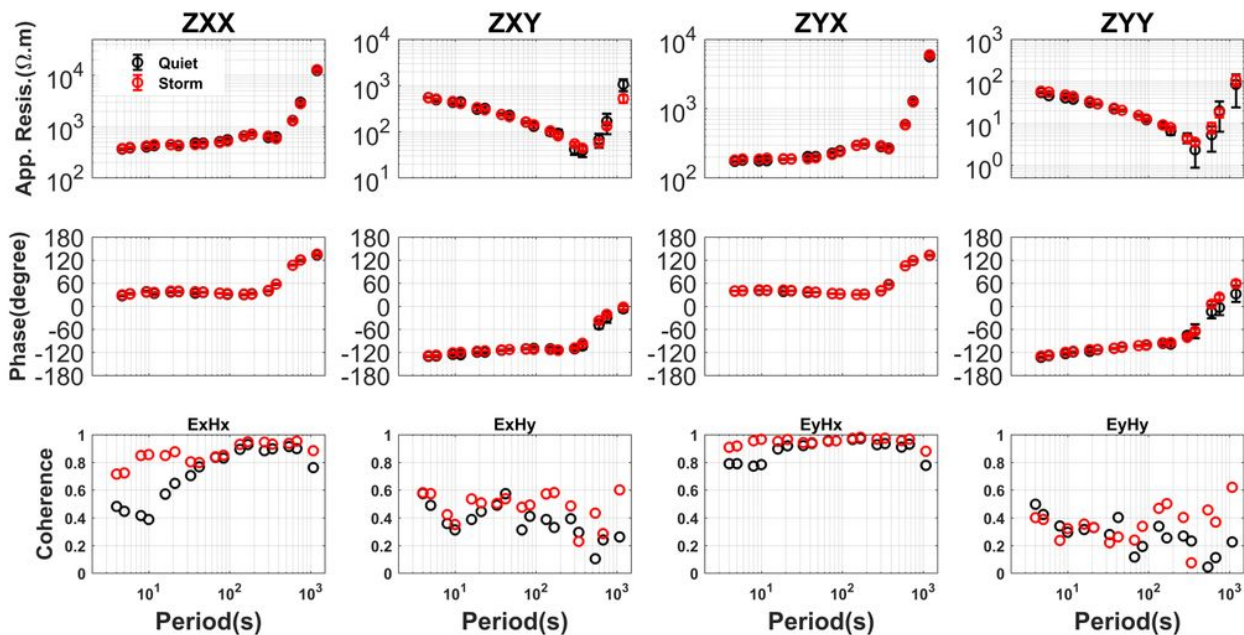


Figure 10

MT sounding curves and coherency distribution during storm days (August 26) and non-storm days (August 23). The black color indicates the results on the non-storm days; the red color indicates the storm day results. The upper figures show the apparent resistivity. The four figures at the middle layer show the impedance phase. The lower figures show the distribution of coherency. The horizontal axis denotes the period in seconds.

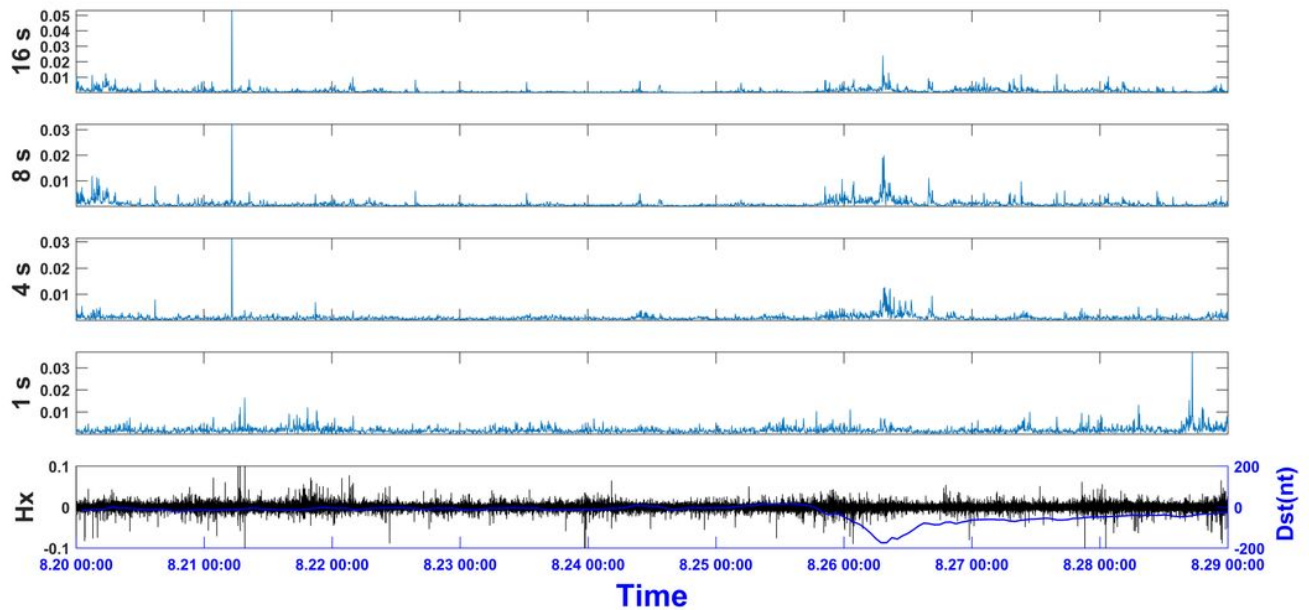


Figure 11

The amplitude variation in periods of 16, 8, 4 and 1 seconds against the Dst index. The upper figure shows the amplitude variation from August 20 to August 28. The lowest figure shows the time variation of the Hx component along with the Dst index variation. The unit of Hx is nT. The horizontal axis denotes the time.

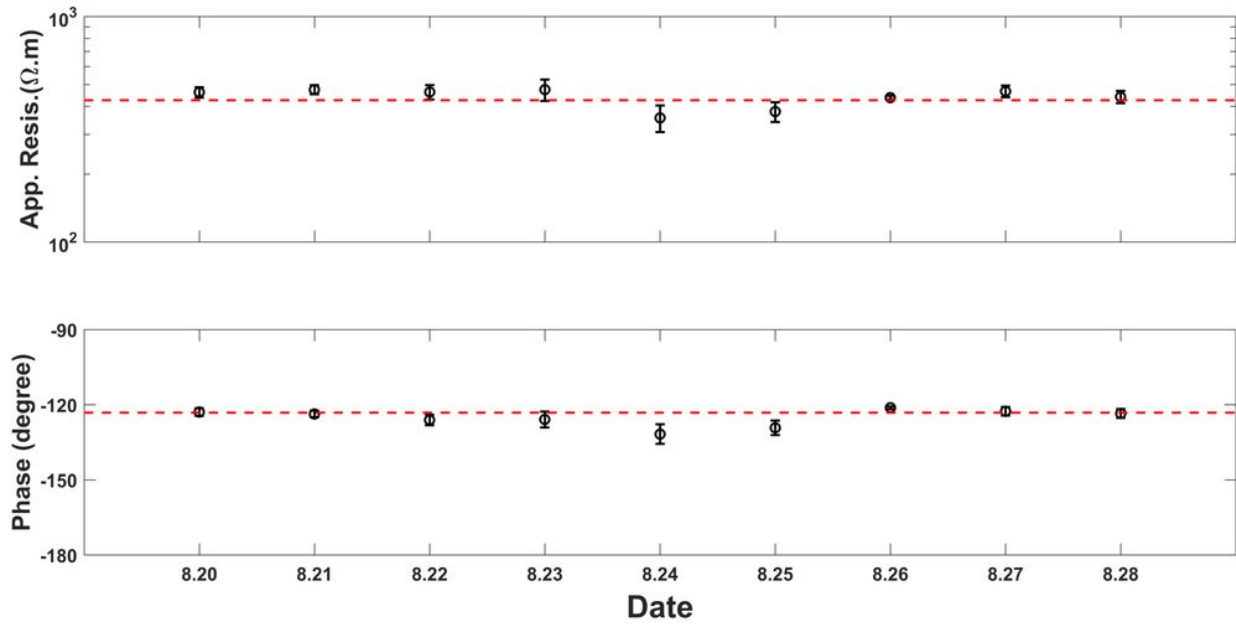


Figure 12

The XY component of the impedance curve was calculated by each day's data at a period of 10 seconds. The horizontal axis denotes the date. The upper figures show the apparent resistivity, and the lower figures show the impedance phase. The red lines show the apparent resistivity and phase calculated by the data from August 20 to August 28.

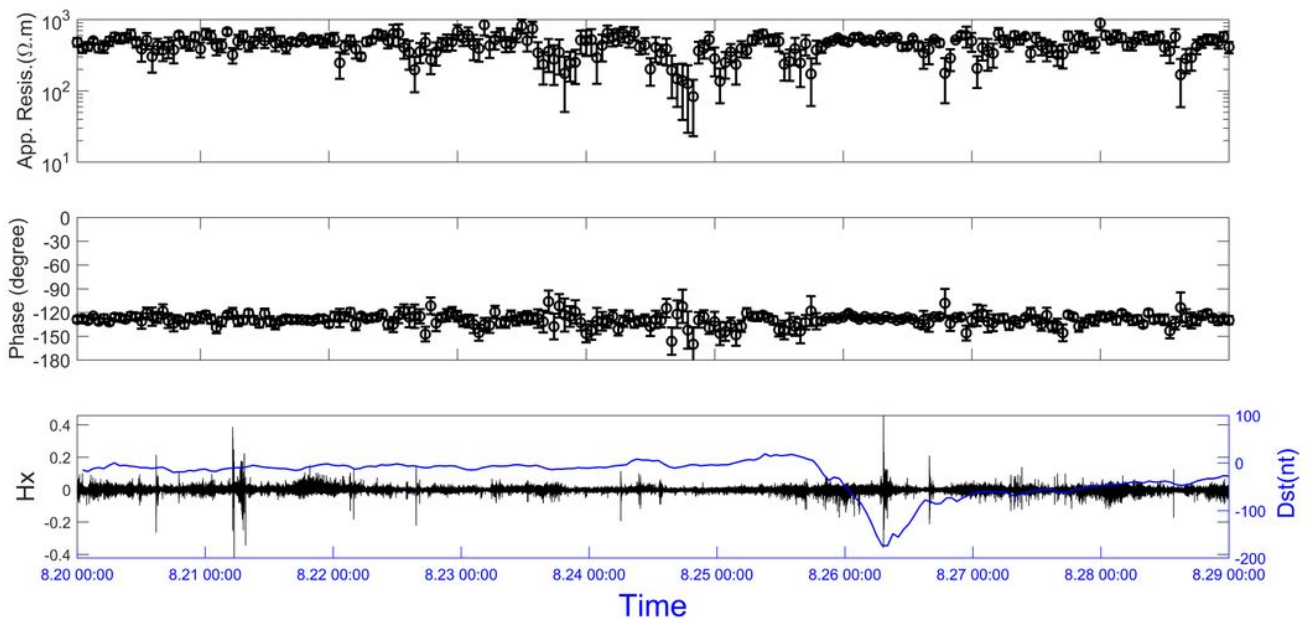


Figure 13

The time variation of the impedance curves calculated using each hour's time-series data at a period of 10 seconds. The horizontal axis denotes the time. One result was calculated using one-hour data. The unit of Hx is nT.

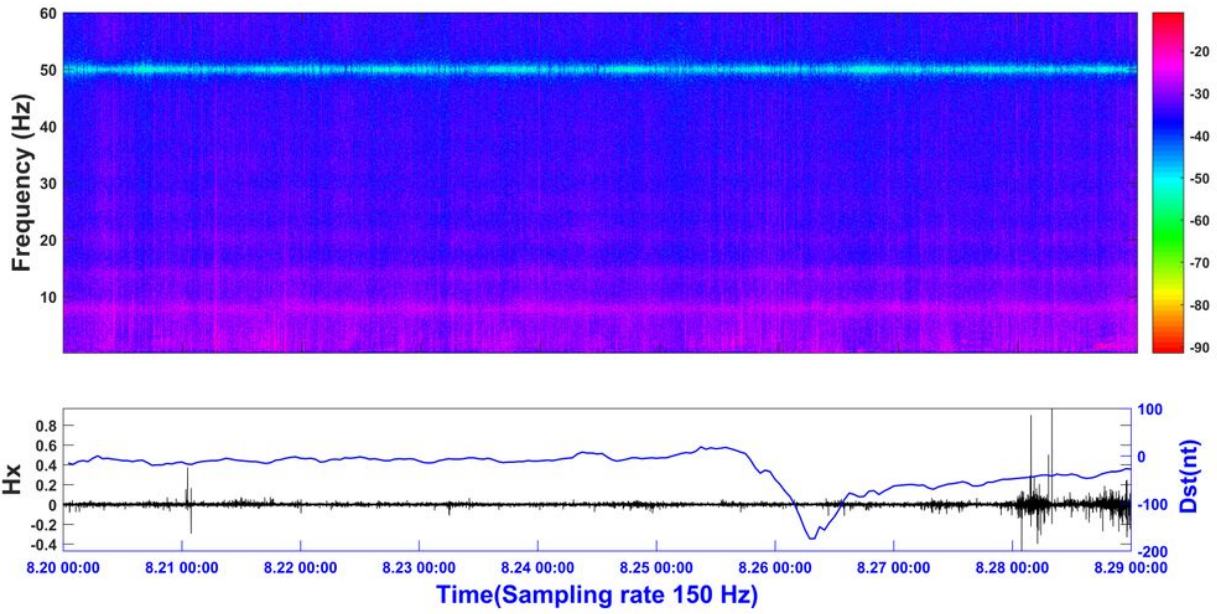


Figure 14

The time-frequency distribution against the Dst index. The sampling rate is 150 Hz. The content is the same as Fig. 9.

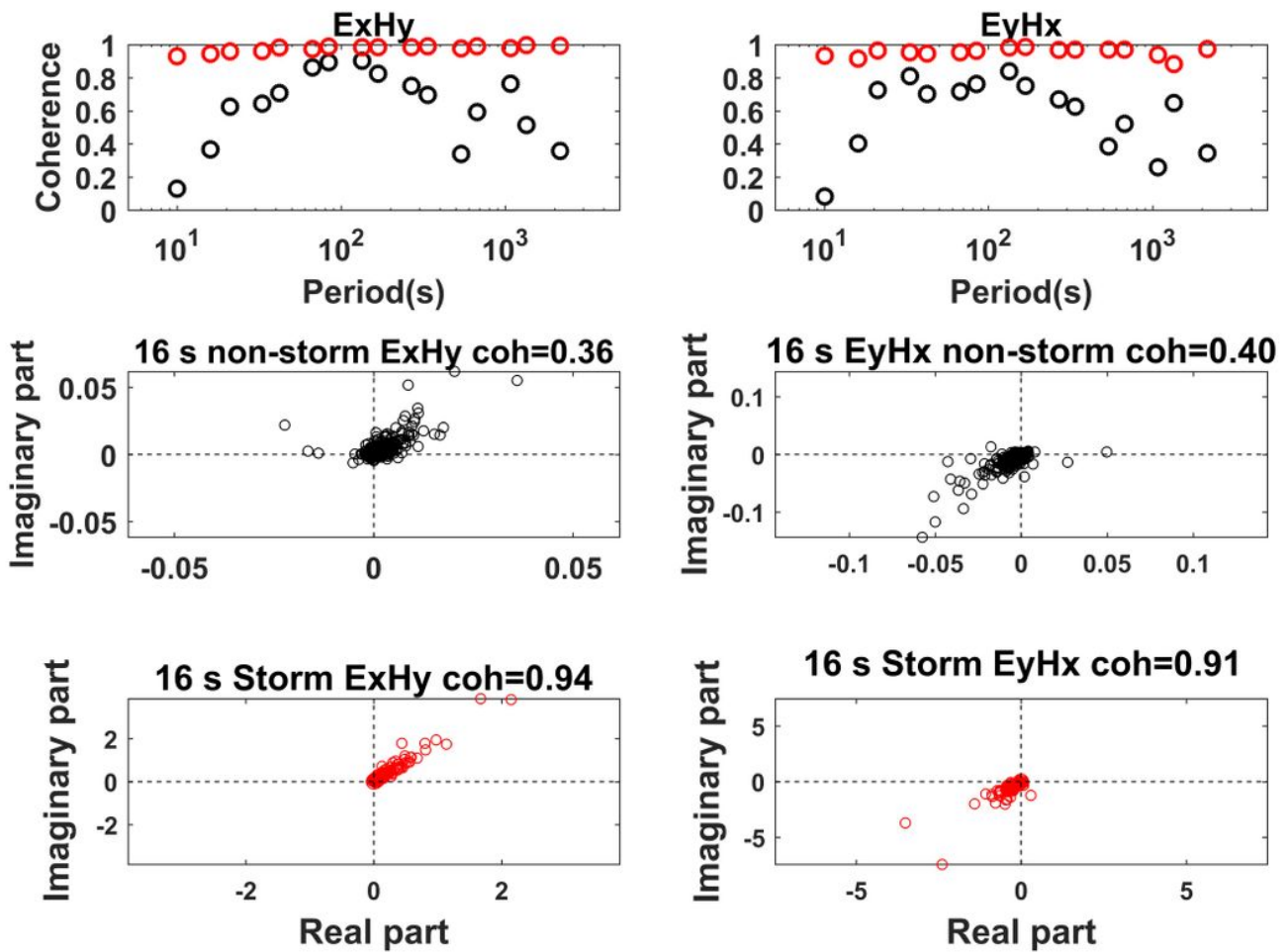


Figure 15

The distribution of coherency in different periods and cross-power spectra at 16-second during the storm and non-storm days. The black color denotes the result using the non-storm data, and the red color denotes the result using the storm data.

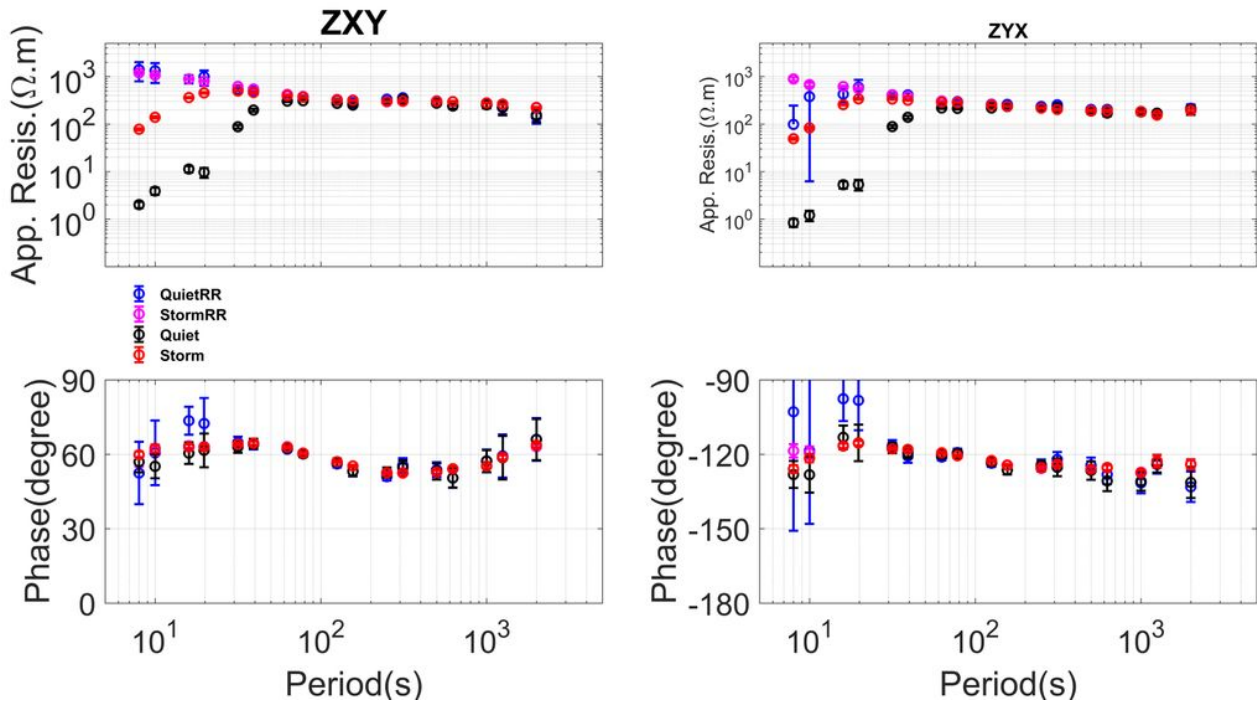


Figure 16

The MT sounding curves using the data observed during storm day and non-storm day. The Quiet result is drawn in black; the QuietRR result is drawn in blue; the Storm result is drawn in red; the StormRR result is drawn in purple.

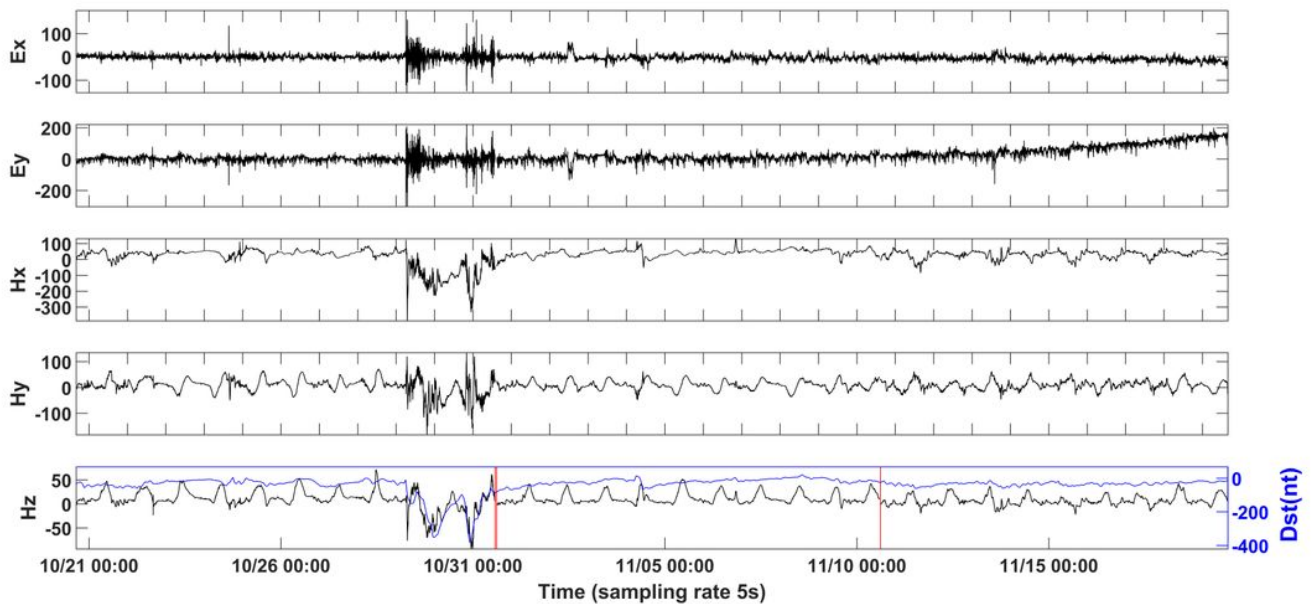


Figure 17

Time-series of MT field data at site 133. The red vertical lines show the data gaps, and the black lines show the 5-component MT data. The blue line shows the variation in the Dst index. The electric field unit is mV/km, and the unit of the magnetic field is nT. The horizontal axis denotes the time in UTC.

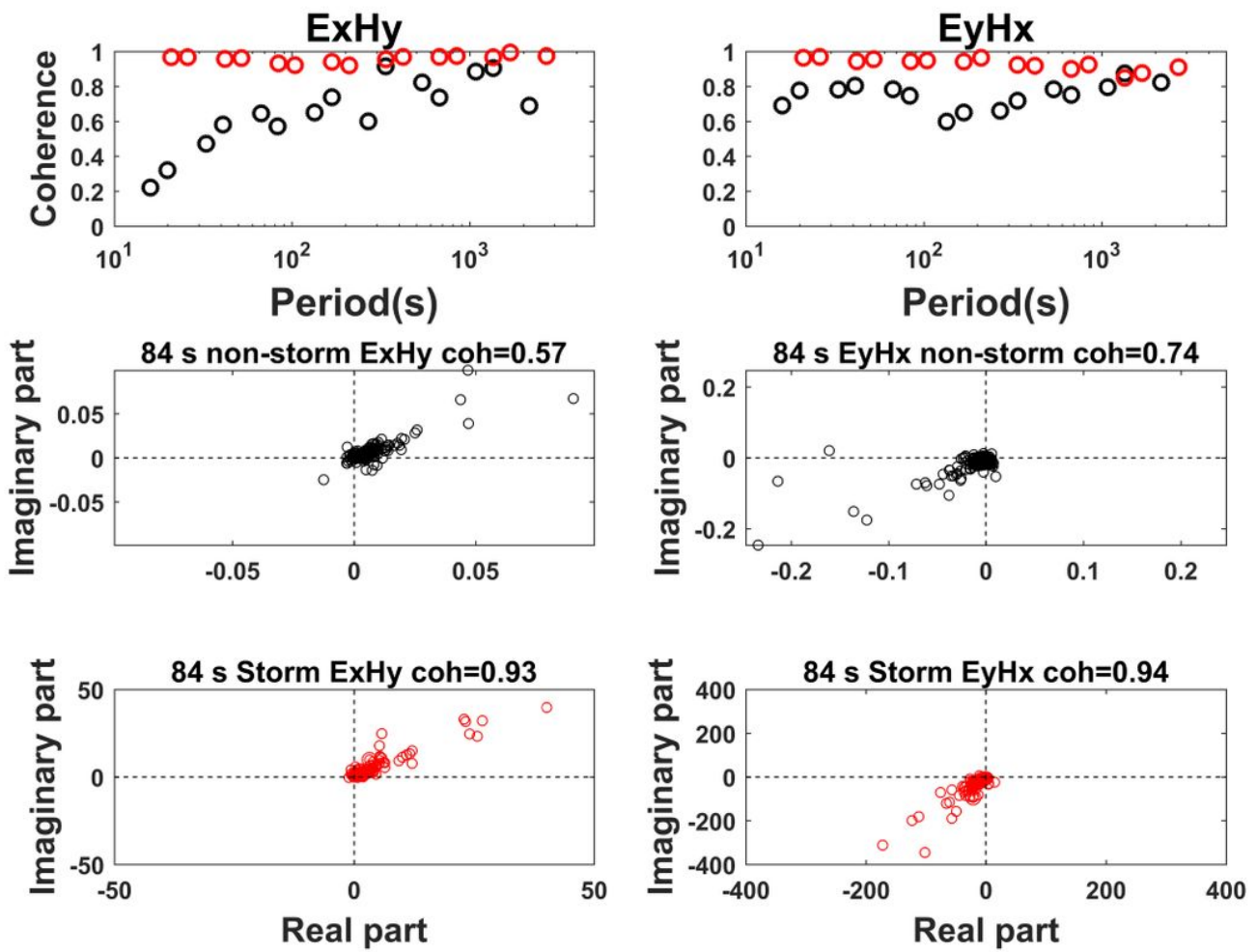


Figure 18

The distribution of coherency in different periods and cross-power spectra at 84 seconds during the storm and non-storm days at site 163.

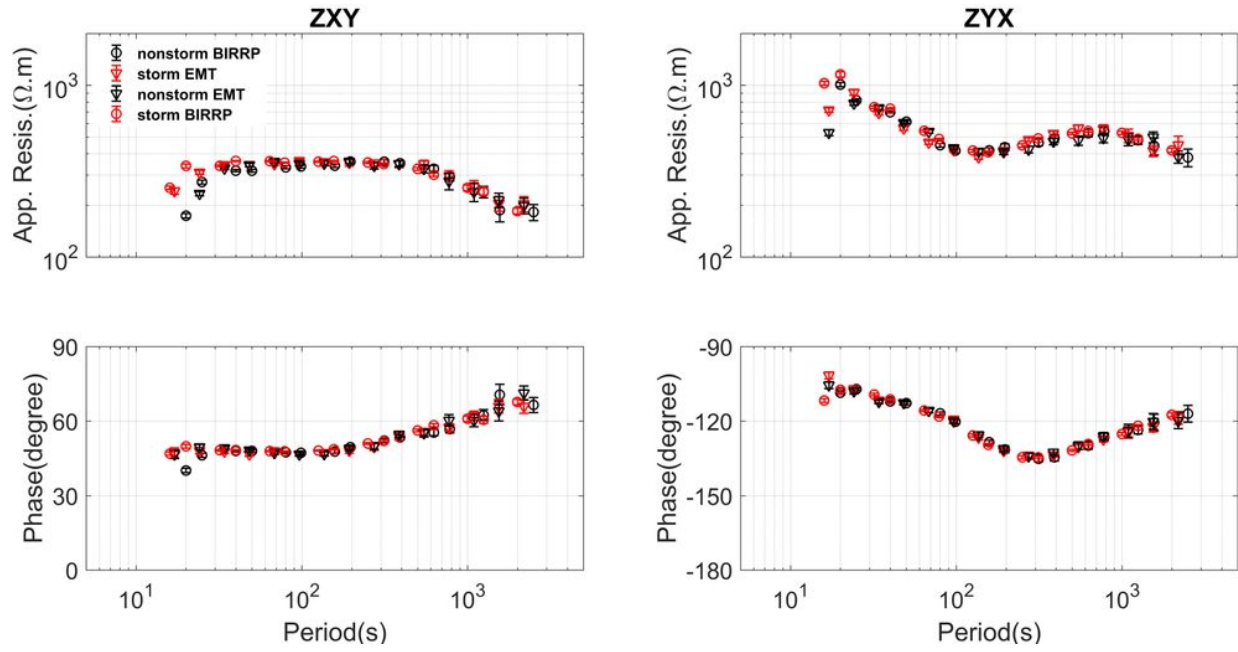


Figure 19

The MT sounding curves calculated using the data observed during the storm and non-storm days at site 163. The triangles denote results calculated by the EMT code; the circles denote the results calculated by the BIRRP.

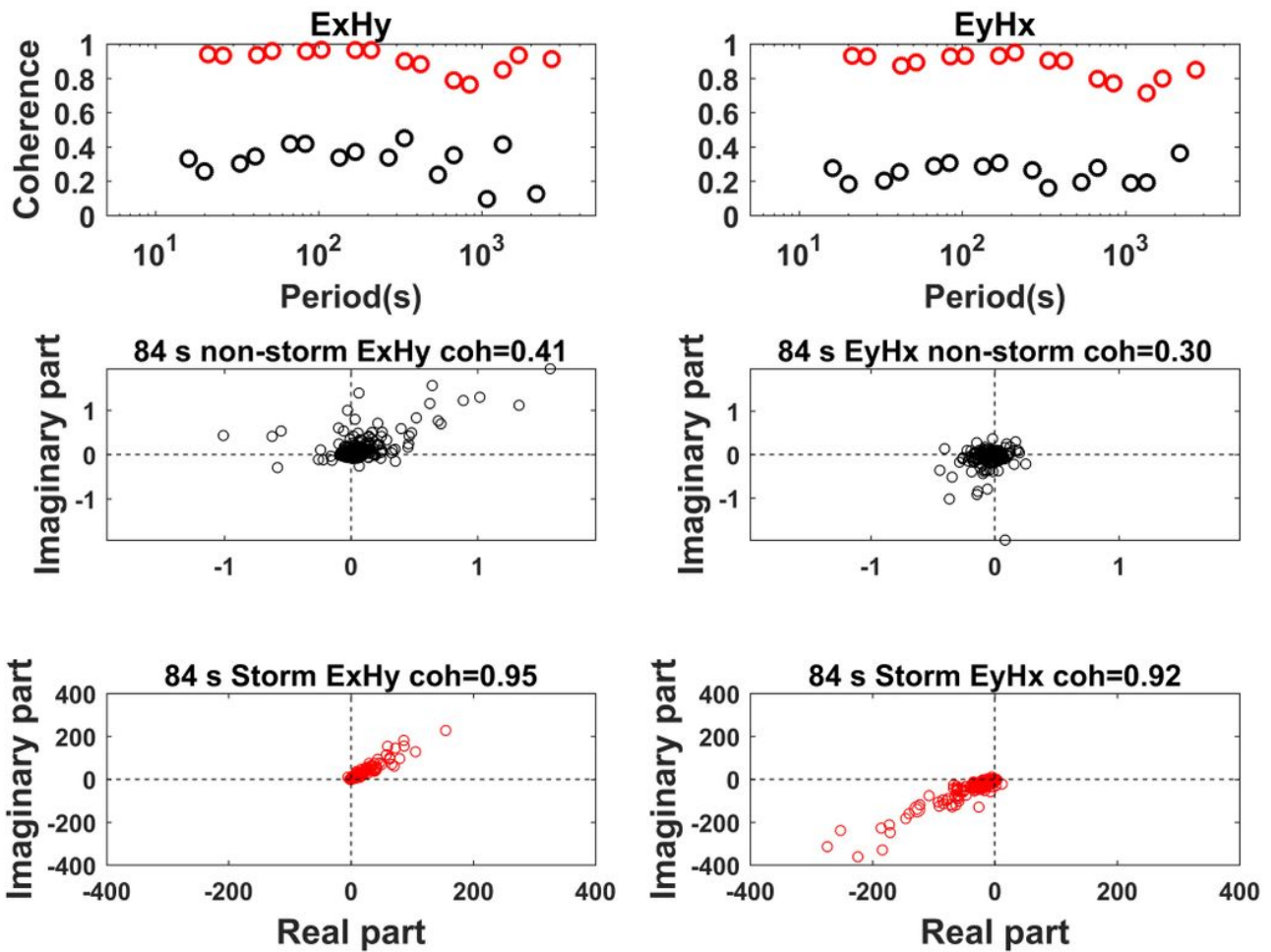


Figure 20

The distribution of coherency in different periods and cross-power spectra at 84 seconds during the storm and non-storm days at site 142. The red color denotes the result during storm days. The black color denotes the result during non-storm days.

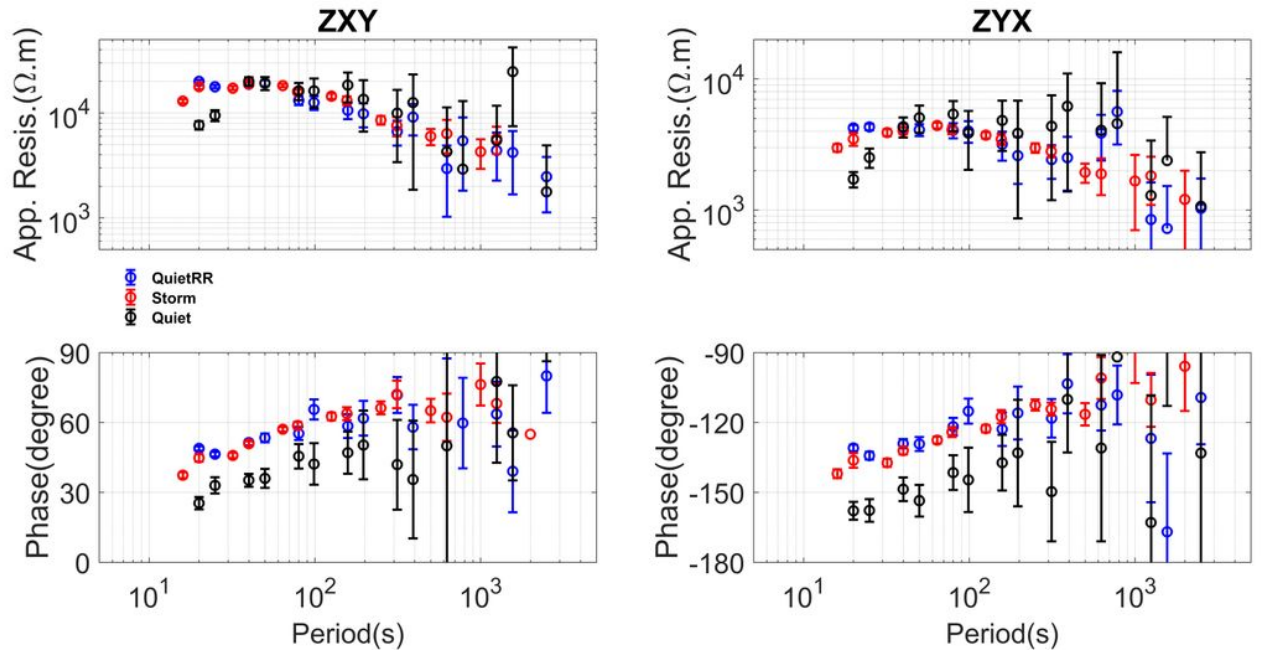


Figure 21

MT sounding curves using the data observed during the storm and non-storm days at site 142. The Storm result is in red. The Quiet result is shown in black. The QuietRR result is shown in blue.

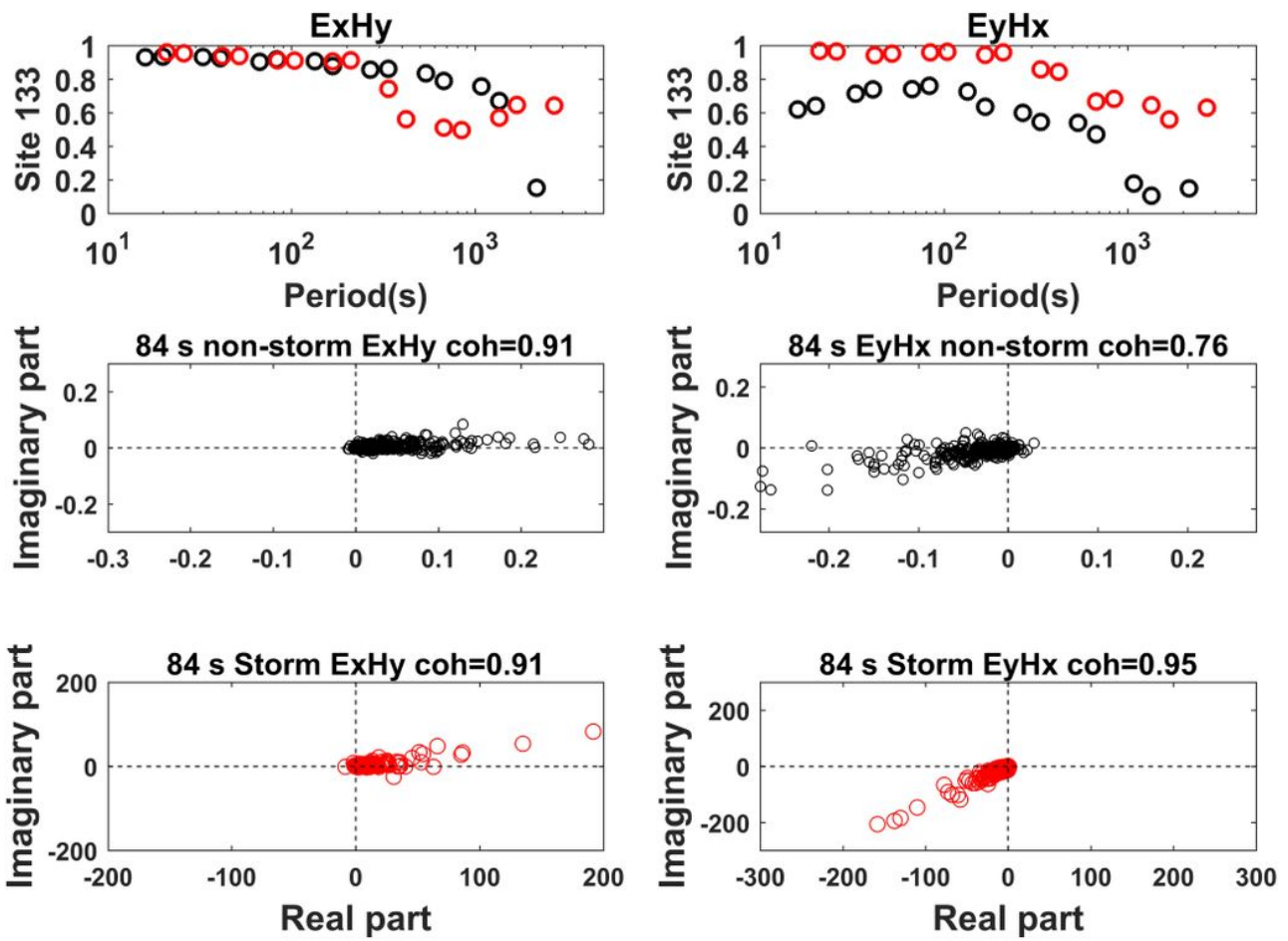


Figure 22

The distribution of coherency across different periods and cross-power spectra at 84 seconds during the storm and non-storm days at site 133. The contents have the same meaning as those in Fig. 20.

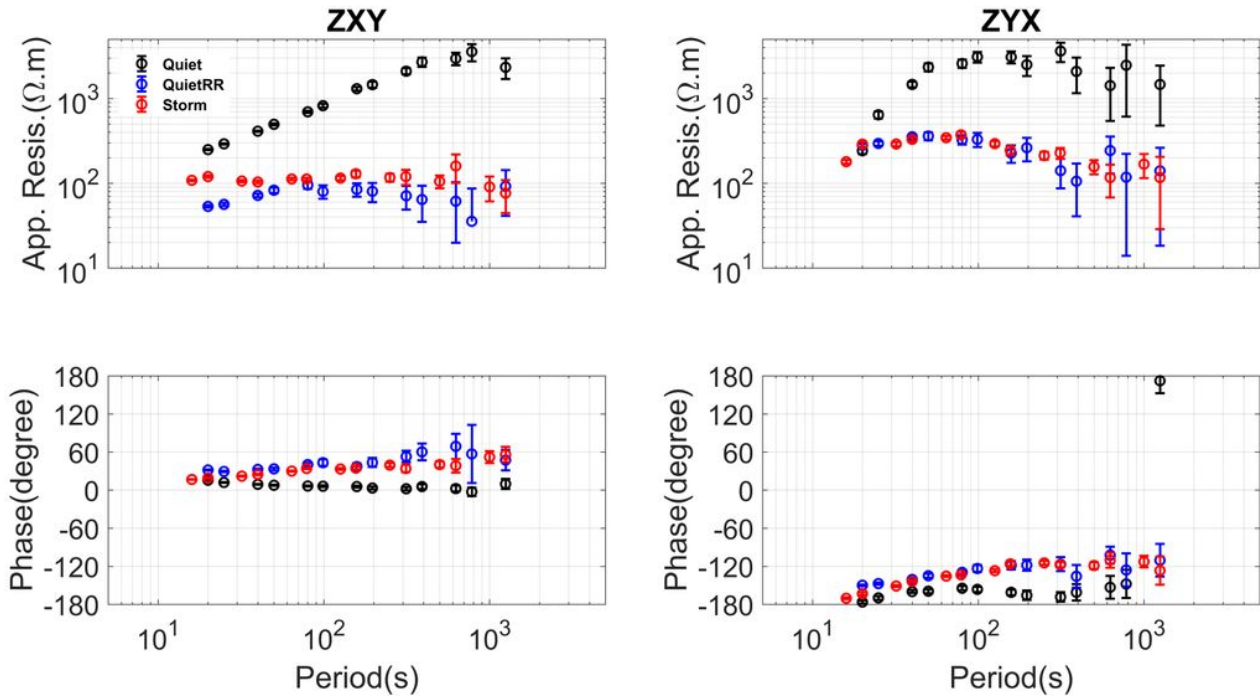


Figure 23

MT sounding curves using the data observed during the storm and non-storm days at site 133. The contents have the same meaning as those in Fig. 21.

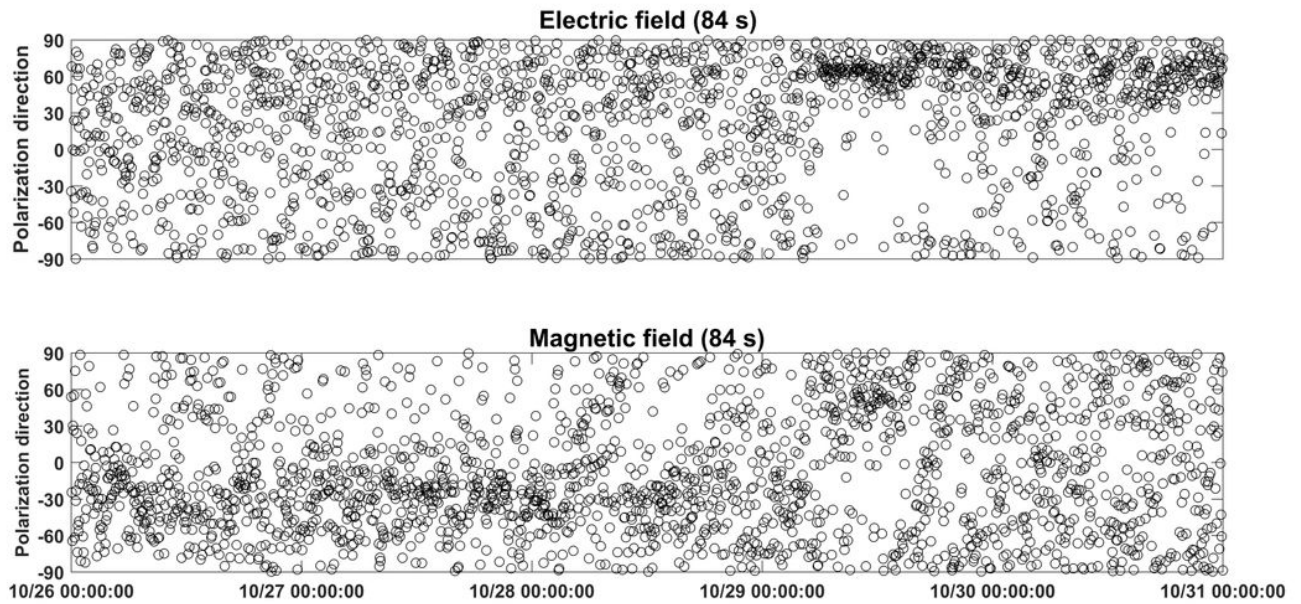


Figure 24

The variation in polarization direction at 84 seconds using the data observed at site 133 from October 26 to October 31. The upper figure shows the polarization directions for the electric field, and the lower figure shows the polarization directions for the magnetic field.

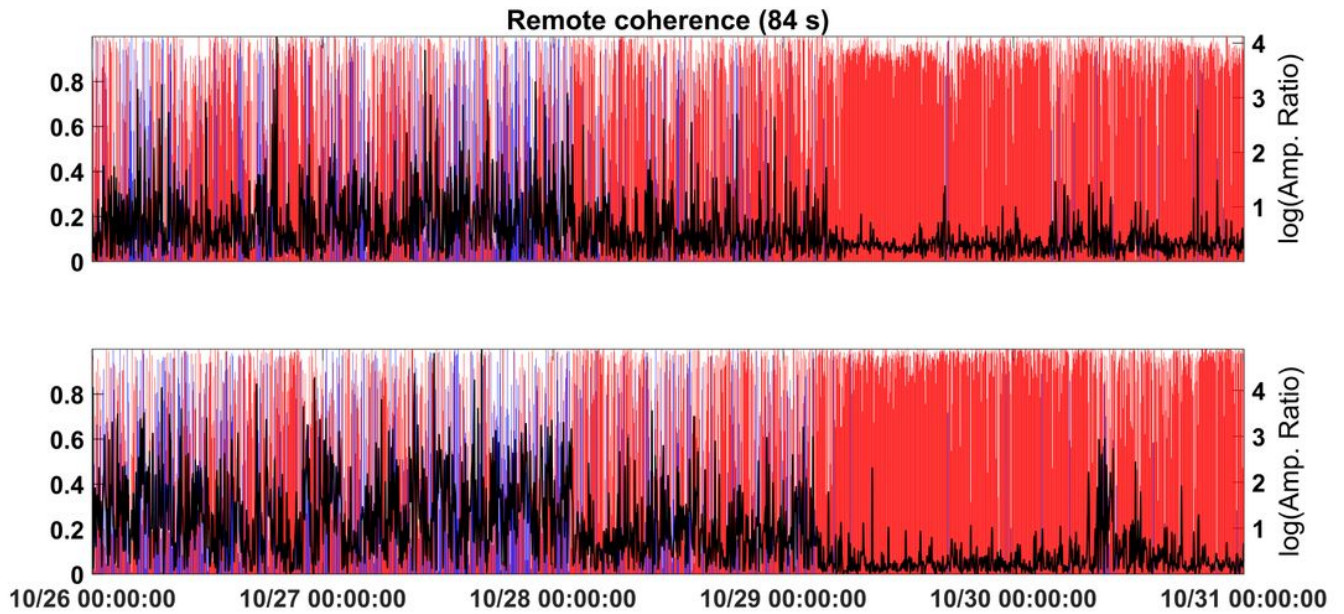


Figure 25

The variation in RLcoh versus R_AR at 84 seconds using the data observed at site 133 from October 26 to October 31. The blue and the red line denotes the RLcoh. Blue indicates a negative value, and red indicates a positive value. The black curve denotes the log value of R_AR.

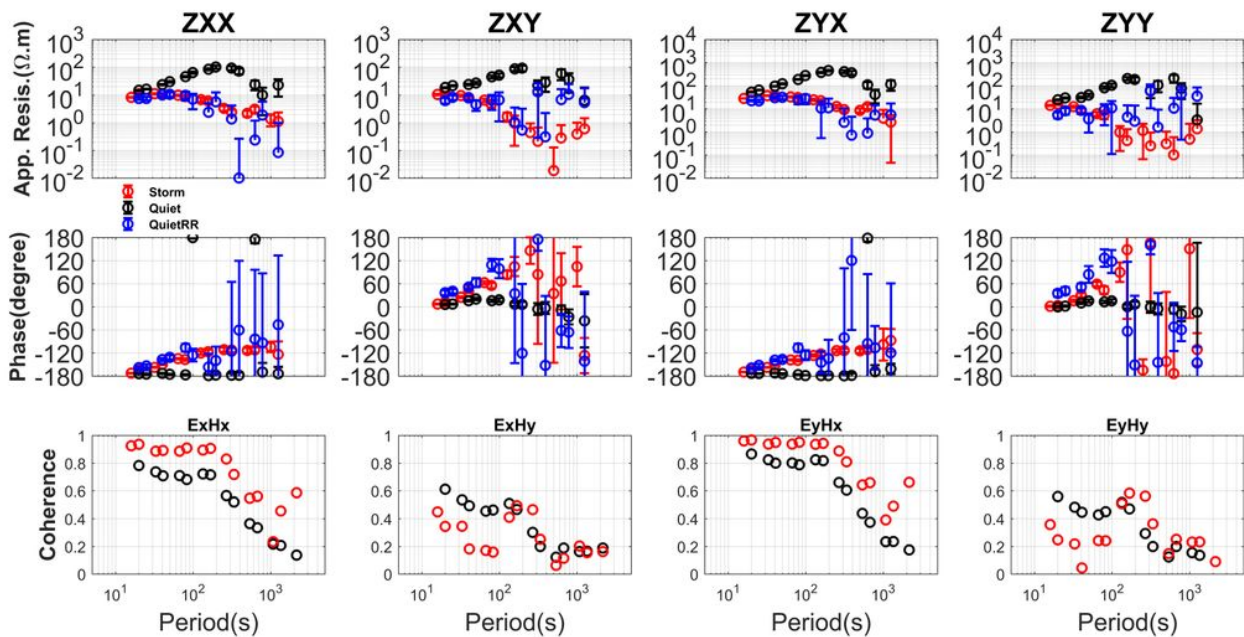


Figure 26

The MT sounding curves and coherency distributions obtained using the data observed during storm days and non-storm days at site 130. The storm result is shown in red. The quiet result is shown in black. The QuietRR result is shown in blue. For coherency, the red color denotes the result during storm days. The black color denotes the results obtained during non-storm days.

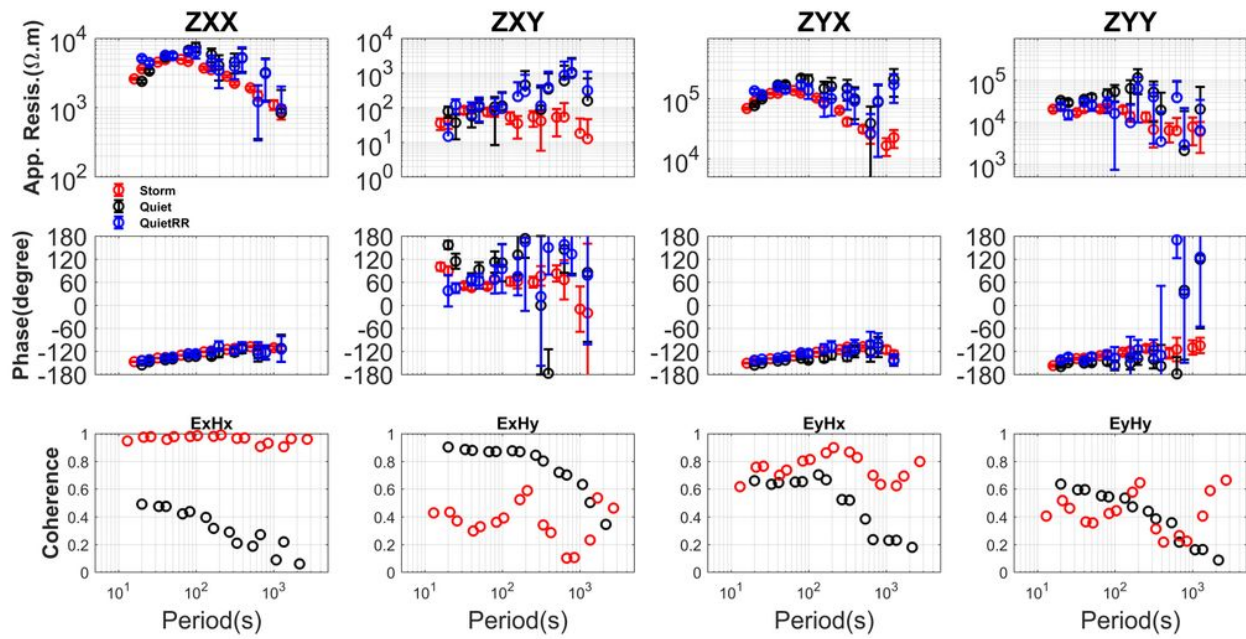


Figure 27

The MT sounding curves and coherence distribution using the data observed during the storm and non-storm days at site 136. The colors have the same meanings as those in Fig. 26.

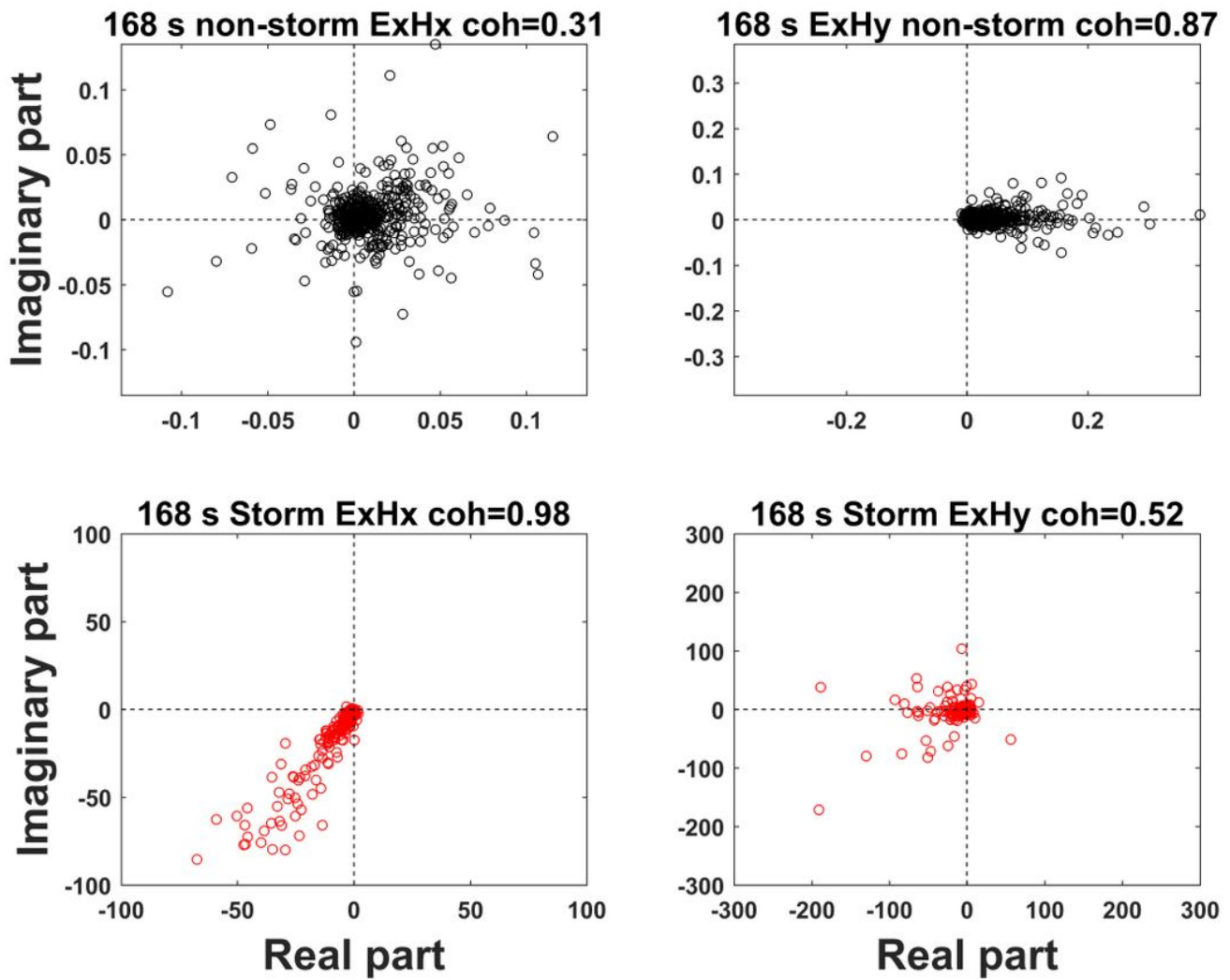


Figure 28

Distribution of cross-power spectra of ExHx and ExHy components at 168 seconds between the storm day and non-storm day at site 136. The colors have the same meanings as those in Fig. 20.

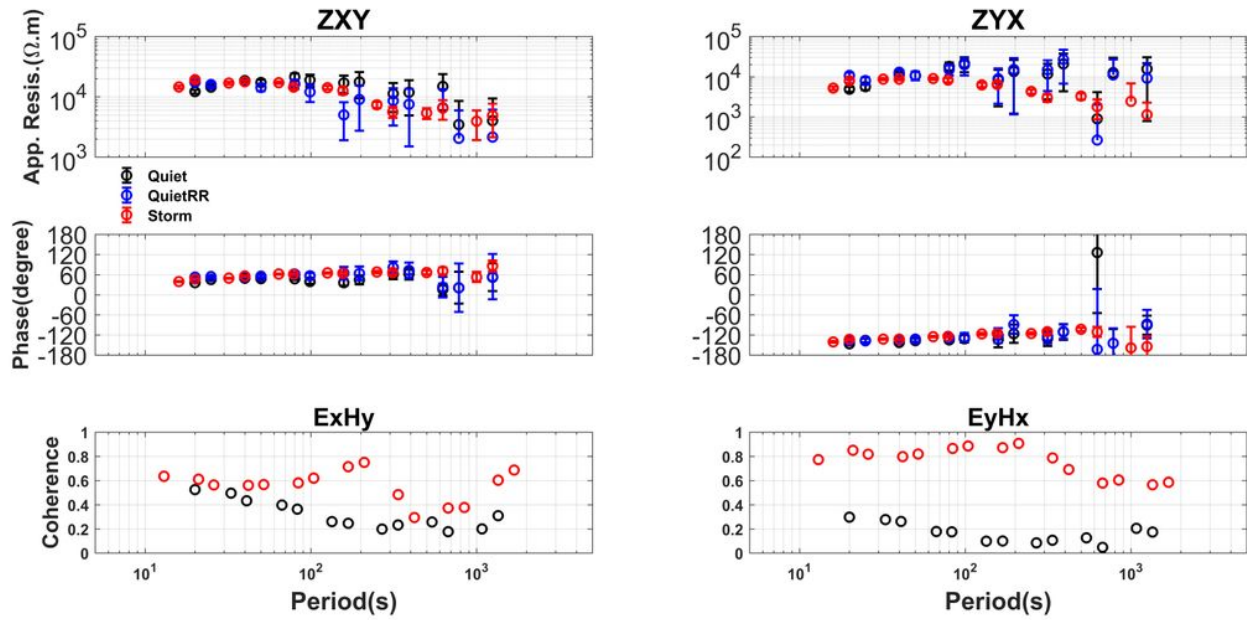


Figure 29

MT sounding curves and coherence distribution using the data observed during the storm and non-storm days at site 139. The colors have the same meanings as those in Fig. 26.

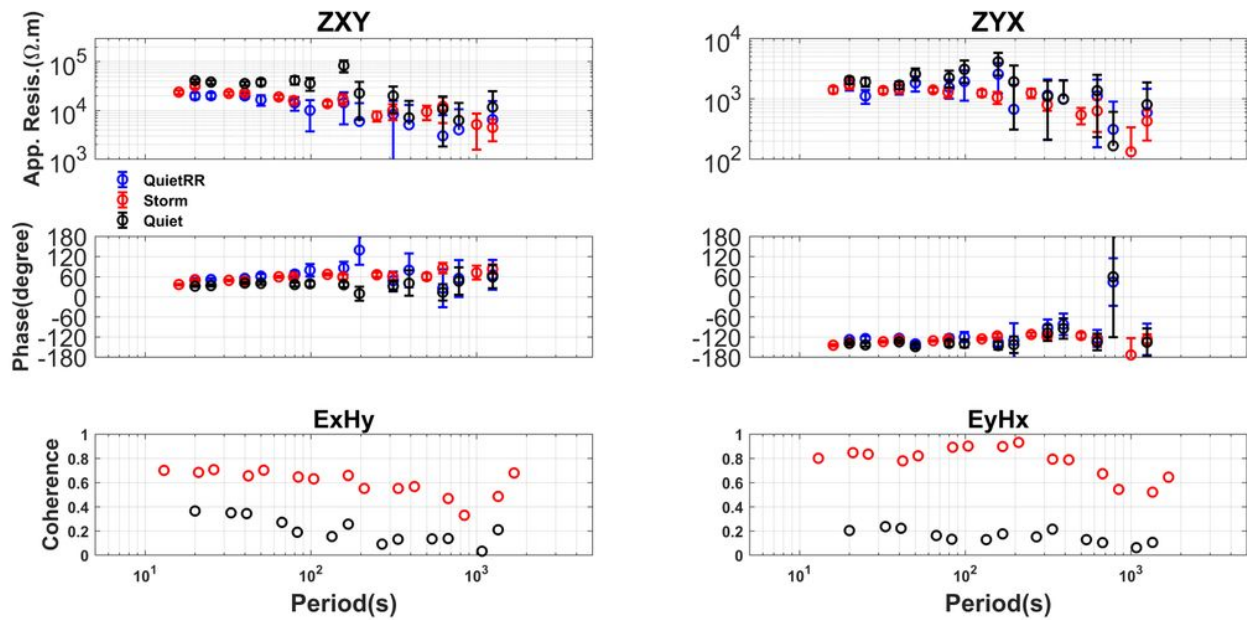


Figure 30

MT sounding curves and coherence distribution using the data observed during the storm and non-storm days at site 145. The colors have the same meanings as those in Fig. 26.

Supplementary Files

This is a list of supplementary files associated with this preprint. Click to download.

- [StormVSnon.jpg](#)